# An Euler-Bernoulli beam model for soft robot arms bent through self-stress and external loads

Gina Olson<sup>a</sup>, Ross L. Hatton<sup>a</sup>, Julie A. Adams<sup>a</sup>, Yiğit Mengüç<sup>a,b,1</sup>

<sup>a</sup>Collaborative Robotics and Intelligent Systems (CoRIS) Institute Oregon State University, Corvallis, Oregon 97331 <sup>b</sup>Facebook Reality Labs Redmond, WA 98052

## Abstract

Soft robot arms remain challenging to model effectively. The arm's primary deformation is bending, coupled with extension or compression, but the strains experienced can be high, the materials are generally nonlinear, and the deformations are large. Existing work has focused on models intended to improve control, which rely on empirical characterization of each arm design, post-manufacturing. This article presents a quasi-static model based on Euler-Bernoulli beam theory that generalizes across a broad set of arm designs. The model is implemented for fluid-driven soft arms constructed with McKibben actuators. Actuators are treated as active materials, and their force is characterized as a nonlinear function of pressure and uniaxial strain. The model is validated for multiple soft arms under external loads, and further use is demonstrated through an investigation of the soft arms' loaded workspace. Higher load capacities are shown to be concentrated at the arms' midlines. Distal taper is examined in an example arm design, and is shown to improve range of motion and load resistance when compared to a constant width arm. The model can be used to evaluate variations on the number and arrangement of actuators in an arm, and it is proposed as a first order design and analysis method for soft robot arms.

Keywords: soft robot, robotics, Euler Bernoulli beam, bending

<sup>&</sup>lt;sup>1</sup>Address all correspondence to this author. E-mail: yigit.menguc@oculus.com.

## 1. Introduction

Soft robotics is motivated by the idea that incorporating a degree of biological softness allows robots to be more adaptable, more robust and more effective. A robotic fish with a soft tail can mimic natural swimming [1], a soft gripper can gently handle fragile reef samples [2] and a soft robot arm can grasp by conforming to an object [3]. Soft robot arms aim to perform reaching and manipulation tasks, but they trade traditional robot arms' high loads and precision for inherent safety and adaptability through conformance. Existing soft robot arms are capable of bending, contraction, extension, or combinations of the these deformations. Each arm's deformation mode, passive compliance, range of motion and applied force are functions of its actuator type and their arrangement.

The workings of soft arms have been established at a high level: contract or extend individual actuators to deform the arm (Figure 1). Qualitative relations between specific design and performance variables (e.g., width vs. passive compliance) can be intuited using existing mechanics models, but the fundamental mechanics of soft arms (e.g., strains experienced, deformation patterns, limiting factors) remain unexplored. There exist no quantitative design rules for soft robot arms that address the interconnections between compliance, force and range of motion.

The softness of soft robots, necessary for compliance and gentle interactions, complicates development of models that can be used to provide design guidance. Soft arms are commonly constructed from nonlinear materials (e.g., elastomers), experience large strains and undergo geometrically nonlinear deformations. Bending, the soft equivalent to traditional rotary joints, receives the most focus. However, existing static and dynamic bending models are limited by narrow applicability, because they rely on experimentally fit parameters that are determined after the arm is built. Using the same parameters under different loading conditions that vary from those tested causes enough inaccuracy to invalidate model use [4]. These parameters have not been demonstrated to generalize across designs. Simple models have been used to predict deformations or aid design of individual actuators [5, 6], despite similar complexities, and there is an opportunity for models that accomplish the

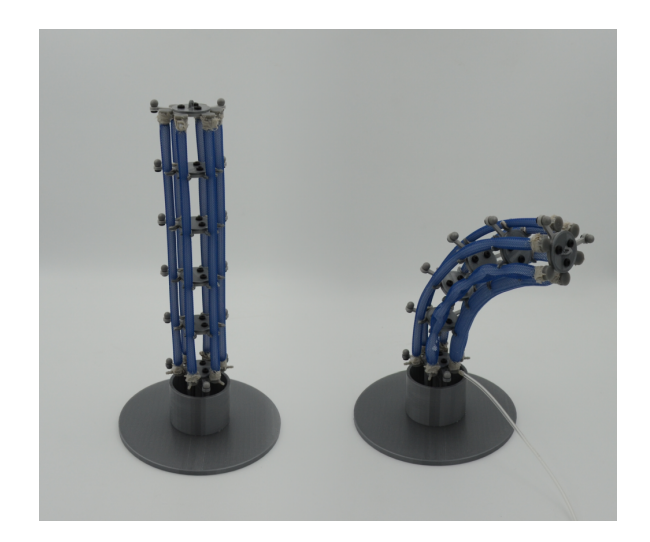


Figure 1: A spatial soft arm. The arm consists of six McKibben actuators equally distributed around a circle. Pressurizing actuators on one side of the arm causes a bend. The bend curvature and direction are determined by the actuators selected and the pressures applied.

same function for soft arms. This article presents a quasi-static bending model derived from a geometrically exact Euler-Bernoulli formulation. This model is generalizable across designs, and it can predict the impact of design changes without constructing and testing an arm, because actuator reaction forces were characterized independently from any soft arm. The model was validated and used to analyze the relationship between arm width and loaded workspace shape, as well as the effect of distal taper on arm performance.

Soft arms have been driven by tendons, shape memory alloys (SMA) or pneumatic actuators [3, 7, 8]. Soft pneumatic actuators employ stiffness asymmetry to turn inflation into a desired motion, whether through fiber reinforcements [6], cross section [9] or material [10]. These actuators may contract, extend, twist, bend or some combination thereof. Pneumatic actuators are popular because they are made from predominantly soft materials, are moderately fast and are cheap and impact resistant [11]. Tendon-driven arms require a stiff backbone, and SMA actuators are comparatively slow [12]. Pneumatically actuated soft arms are the focus of this manuscript, and the potential for expanding the model to other actuator types is discussed in Section 6.

Although individual bending actuators exist, soft arms tend to be constructed by com-

bining contracting or extending actuators to form bending units. The detailed design of each arm is different, but most soft arms follow a standard schema. Longitudinal actuators are arranged in parallel, either in a plane to bend left or right (Figure 2) or distributed evenly around a circle to bend in any direction (Figure 1) [3, 13–18]. Arms constructed with contracting actuators bend toward the pressurized actuators, while arms constructed with extending actuators bend away. Multiple bending units can be connected serially in order to increase the number of degrees of freedom.

Modeling efforts for robot soft arms have focused on kinematics and dynamics for model-based control, rather than modeling to aid design. Kinematic models use sensor input (e.g., actuator length) to geometrically relate known deformations to arm shape [19, 20]. These models are well suited to arms where actuators' lengths are simple to measure in situ, and for closed loop control, but the models do not predict the results of design changes such as altering the arm's width. Dynamic models have been formulated with Euler-Langrage equations, but these models simplify stiffness parameters to constant values experimentally fit for each arm [4, 15, 21]. Experimental stiffnesses improve accuracy and solution speed, which is beneficial for model-based control but invalidates model use for design. Recent models have used Cosserat rod theory to add shear and torsion to the arm's kinematic representation, but these models were either derived for cable-driven arms, which have a simpler actuation force profile [22], or use linear elastic material models that do not model the fundamental behavior of pneumatic actuators [23].

Static or quasi-static modeling efforts have made more progress toward generalizability. Classical bending models are limited to small strains and deformations, but they can be extended to geometrically exact (i.e., large deformation) if closed-form solutions are not required. Euler-Bernounlli formulations have been developed for bending actuators, but the formulations rely on linear elastic materials and do not extend to the complexity of actuators in arms [10, 24]. Static models developed for cable-driven and shape memory alloy arms also rely on material models that do not generalize to the more complex case of soft pneumatic actuation [7, 25]. Static models of pneumatically-driven soft arms have used simplified actuator models [26], which limit their accuracy, and have assumed that the

neutral axis lies at the arm's midline [17].

Soft bending arms are mechanically similar to beams with active elements that change length and stiffness through self-stress applied during pressurization. Euler-Bernoulli beam theory requires a planar cross section, but many arm designs incorporate reinforcing plates that limit perpendicular shear [4, 14]. Linear elastic material constants used in balance laws can be replaced by actuator force characterizations. Prior work derived an Euler-Bernoulli model for soft bending arms, which was generalizable across designs but excluded external loads [27].

This manuscript extends the previous model to include external loads, which requires a more thorough actuator characterization and nonconstant curvature kinematics. The developed model is the first validated, generalizable model of fluid-driven soft arms. The contributions of this work are:

- A model for soft arm bending that generalizes across designs, and can be used to examine the comparative load capacity and curvature of design variants prior to arm manufacture.
- Model validation for load-free and loaded planar and spatial arms.
- Closed form relations for curvature and bend direction for structurally minimal unloaded arms.
- Analysis of how external loads affect soft arms' workspace.

Section 2 defines the arm design schema and presents the details of the validation test arm. The extended model is presented in Section 3, and further details on actuator characterization are given in Appendix A. The model is validated for planar and spatial arms in Section 4. The effect of segment width and arm distal taper on applied force and range of motion is analyzed in Section 5. Section 6 concluded with comments on the model's potential and limitations, as well as future work.

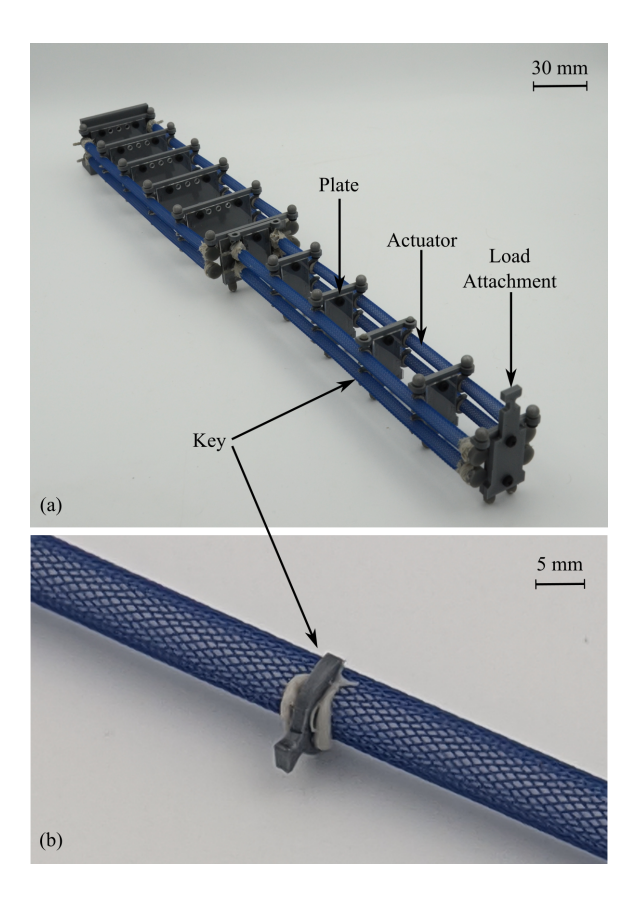


Figure 2: (a) A two segment planar soft arm that demonstrates the modular architecture. McKibben actuators are non-permanently attached to plates via entrapped keys. The plates determine segment width. The keys are shown on a lone actuator in (b). Plates and keys were 3D printed with polylactic acid filament. Keys were attached to actuators with Momentive RTV157.

## 2. Soft Arm Design

The soft arms are constructed from longitudinal pneumatic actuators connected by rigid plates (Figure 2). Similar arms can be constructed from contracting or extending pneumatic actuators, but the model was validated with arms composed of contracting McKibben actuators. The actuators consisted of a polyester plastic braided sheath (McMaster #9284K2) over an EcoFlex 00-30 elastomeric tube. Each actuator was initially 7 mm in diameter and 230 mm long. The sheath expands radially and contracts in length when inflated.

The actuators were joined to the rigid plates via a previously-developed modular key system [28]. The keys were permanently bonded to the actuators with RTV157, and non-

permanently entrapped within cutouts in the plates. The rotational stiffness of the bonded joint and the entrapped joint is high, such that the joint cannot pivot freely. The plates define actuator spacing and arrangement, and also enforce cross section planarity and increase the arm's buckling load. Arms were constructed with either planar architectures (bending left or right in a single plane) or spatial architectures (bending in any direction by pressurizing two actuators in specific proportions). Segments were connected by screws between plates.

Five planar segment widths were evaluated: 20 mm, 30 mm, 40 mm, 50 mm and 60 mm. The model was also validated for a two segment planar arm, with a 60 mm base width and a 30 mm tip width, and a single-segment spatial arm with a 40 mm diameter. The spatial arm had six actuators spaced evenly around the circular perimeter. Multisegment spatial arms were not considered as part of this initial validation and analysis effort.

The longitudinal-actuator arm design is representative of a broader class of soft robot arms. Similar designs connect longitudinal actuators to rigid plates [4, 14], or replace plates with ties around or chemical bonds between bundled actuators [3, 29]. While the presented model generalizes across arms designs, each actuator design must be characterized in order to be used.

# 3. Bending Model

The model considers arms composed of N parallel pneumatic actuators, a subset of which are pressurized. Actuator arrangement is known, as are external loads, and the model determines the arm's deformed shape. The formulation describes arm shape with shear-free curvatures at the arm's neutral axis, like Euler-Bernoulli beams, and the formulation is geometrically exact (i.e., it does not restrict deflections to one dimension). Solutions must be determined numerically, but the model can accommodate high strains and large deformations. While the model can be formulated as coupled, nonlinear differential equations, similar to existing rod theory [30], it is presented as a set of equilibrium equations that are discretized along arm length and solved numerically.

## 3.1. Segment model derivation

The segment model replaces linear elastic constitutive relations ( $\sigma = E\varepsilon$ ) used in Euler-Bernoulli beam models with discrete, summed actuator forces. A soft actuator's reaction force depends on pressure, P, and strain,  $\varepsilon$ , and throughout the model derivation this force is abstracted as a general relation  $F = F(P, \varepsilon)$ . Soft arms use pneumatic actuators as primary movers and support structures, and actuator reaction force models must be equally holistic. Actuator models typically focus on the actuation region, which for McKibben actuators is the set of strains and pressures that produce a tensile force at a contraction strain [5, 31, 32]. No physical limitation keeps actuators within the actuation region, and certain combinations of self-stress and external load can strain actuators beyond it. This complexity is hidden by the abstracted relation  $F(P,\varepsilon)$ , but the model requires a characterization that is continuous and accurate across the relevant strain and pressure domains. Actuator characterizations are discussed in Section 3.2, and the characterization functions are provided in Appendix A.

The segment model's assumptions are:

- 1. The initially planar cross section remains planar. Shear normal to the neutral axis is neglected, and strains are assumed to be linear through the cross section.
- 2. Actuators' forces act as point loads. Each actuator's reaction force at a given point is represented as a point load applied at the actuator cross section's center. Actuator strain is assumed to be perfectly uniaxial.
- 3. Actuators behave identically along their length. End effects and local disturbances near keys are neglected. The characterization  $F(P, \varepsilon)$  applies regardless of length.
- 4. The arm bends in one plane and loads are applied within that plane. The orientation of the plane may be initially unknown, and is determined through moment equilibrium, which is selected to be evaluated at the arm's base. Planar arms follow this assumption inherently, whereas spatial arm bend direction is modeled by a single angle.
- 5. Arm deformation is quasi-static and history independent. Hysteresis, viscoelasticity and dynamics are neglected.

The model is presented for a single segment of a spatial arm (Figure 3) under a tip load

Q. The arm cross section consists of N identical actuators, and pressurizing two actuators provides directional control. Pressurized actuators need not be adjacent. The arm is assumed to bend in a single plane, at an angle  $\theta_b$  from a reference plane. The angle  $\theta_b$  depends on the actuators selected and pressures applied. The derivation steps are to (1) establish kinematics, (2) determine reaction forces and (3) apply equilibrium relations.

Kinematics. The arm segment is modeled kinematically using the same assumptions as Euler-Bernoulli beam theory, which is equivalent to a shear-free, torsion-free, planar Cosserat

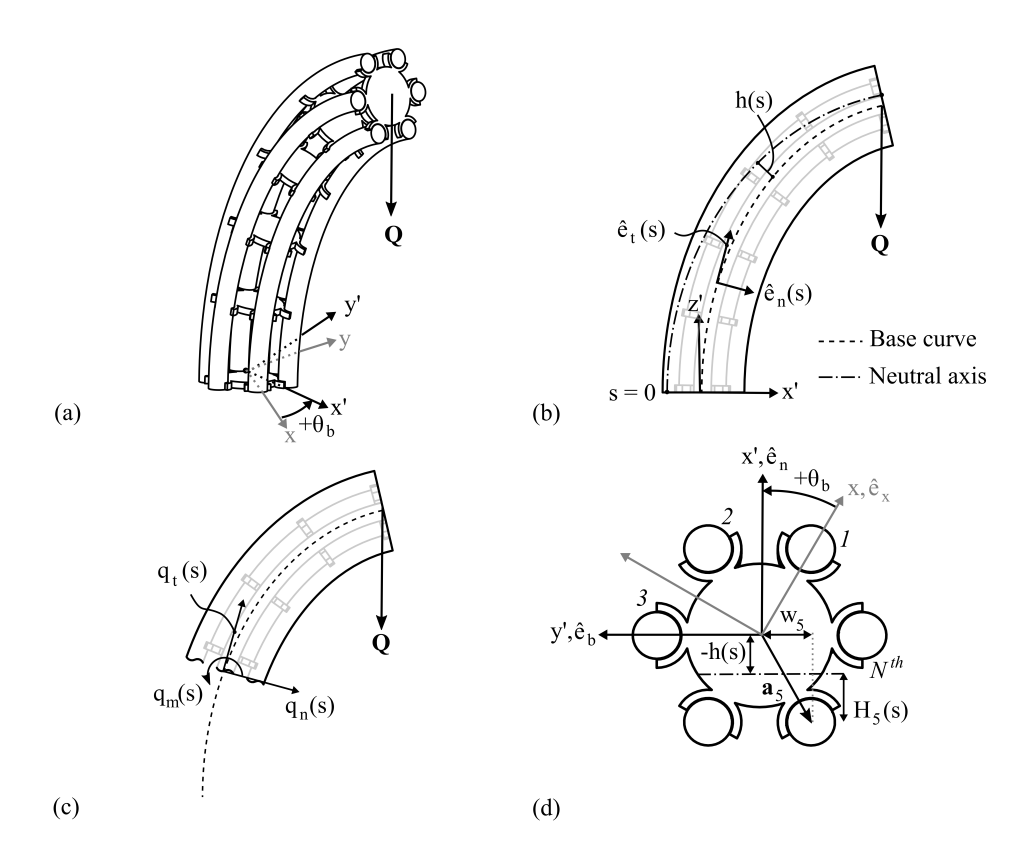


Figure 3: Notation definition. (a) The arm exists within a Cartesian coordinate system and bends within a single plane rotated by  $\theta_b$  from the x-z plane. (b) The bend within the rotated plane x'-z' can be described by either a neutral axis height h(s) and curvature  $\kappa_{NA}(s)$ , or a base curvature  $\kappa_c(s)$  and base curve stretch  $\lambda_c(s)$ . (c) Each point along the arm has an internal reaction with a normal component  $(q_n(s))$ , tangent component  $(q_t(s))$  and moment  $(q_m(s))$ . (d) The cross section forces and moments at each point s are determined by each actuator's distance from the neutral axis and arm midline. The neutral axis height, h(s), is illustrative as negative, which reflects many of the validation case results.

rod. The planar cross-sections remain planar and rigid throughout deformations of the structure, per the shear-free assumption. Curvature lies in a single plane, which assumes that the shapes the segments assume under the applied loads (pure forces at the end of the arm, and the corresponding force-moment couples induced at the interfaces between segments) are close enough to planar deformations that out-of-plane effects can be neglected.

The arm is straight in the segment's neutral configuration (no external load and no pressure to the actuators), and its cross-sections can be parameterized by their distance s from the base of the segment in this configuration. There is a frame  $\{\mathbf{e}_x, \mathbf{e}_y, \mathbf{e}_z\}(s)$  at the center of each cross section, for which  $\mathbf{e}_z$  is normal to the cross section,  $\mathbf{e}_x$  points to Actuator 1, and  $\mathbf{e}_y$  is in the cross section at right angles to  $\mathbf{e}_x$ . The frame at the proximal end of the segment (s=0) provides an xyz frame for describing the geometry of the entire segment (see Figure 3). Each actuator passes through the cross-sections at a location  $a_i = \begin{bmatrix} a_{ix} & a_{iy} & 0 \end{bmatrix}^T$ .

There are two methods of describing the segment's deformed shape. Euler-Bernoulli beam theory traditionally describes deformations using the curvature and location of the beam's neutral axis, or set of cross sectional locations with zero strain. Other formulations, like Cosserat rod theory, use curvature and stretch of a base curve. Both formulations are developed in this manuscript. The neutral axis formulation is presented in Appendix B, and the base curve formulation is presented in this section.

The base curve formulation describes the segment's deformed shape by three quantities: the *bend plane* of the "base curve" of the segment (the curve running through the centers of the cross-sections), the base curve's *stretch* and the base curve's *curvature*:

- 1. The bend plane x'-z' is rotated from the x-z plane at the proximal end of the segment by an angle  $\theta_b$  around the z axis. The bend axis y' is the orthogonal complement to the bend plane.
- 2. The stretch  $\lambda_c(s)$  is a geometric (proportional) expression of the extension ( $\lambda_c > 1$ ) or compression ( $\lambda_c < 1$ ) of the base curve, and corresponds to the speed at which a point moving along the deformed curve at  $\dot{s} = 1$  travels as measured in the x' z' frame. Stretch  $\lambda_c(s)$  is related to the strain  $\epsilon_c$  in the base curve as  $\lambda_c = 1 + \epsilon_c$ .

3. The curvature  $\kappa_c(s)$  is the rate at which the tangent vector to the base curve rotates as a point moves along the curve at unit speed as measured in the ambient space, or within the world, and its inverse is the local radius of curvature of the base curve. A closely-related quantity is the s-curvature,  $\kappa_s$ , where

$$\kappa_s = \kappa_c(s)\lambda_c(s) = \frac{d\theta}{ds},$$
(1)

which is the rate at which the tangent vector rotates as a point moves along the curve at unit  $\dot{s}$  speed.

The locus of the base curve in the bend plane and its tangent, for a given stretch and s-curvature, can be generated as the solution to

$$\begin{bmatrix} z' \\ x' \\ \theta \end{bmatrix} (s) = \int_0^s \begin{bmatrix} \cos \theta(S) & -\sin \theta(S) & 0 \\ \sin \theta(S) & \cos \theta(S) & 0 \\ 0 & 0 & 1 \end{bmatrix} \begin{bmatrix} \lambda_c(S) \\ 0 \\ \kappa_s(S) \end{bmatrix} dS, \tag{2}$$

in which the third row integrates  $\kappa_s$  to find the tangent orientation at each point along the curve, and the first two rows use this tangent orientation to direct a translational flow at speed  $\lambda_c$ .

The shear-free assumption implies that the cross-sections are arranged along the base curve such that their  $\mathbf{e}_z(s)$  axes are aligned tangent to the base curve. The arm is torsion-free, which means this alignment is achieved by rotating each cross-section frame around the y'-axis by  $\theta(s)$ . The orientation R(s) of the cross-section frames relative to the xyz frame at the proximal end of the segment is the composition of the bend-plane and bending rotations,

$$\begin{bmatrix} \mathbf{e}_x & \mathbf{e}_y & \mathbf{e}_z \end{bmatrix} = \begin{bmatrix} \cos \theta_b & -\sin \theta_b & 0 \\ \sin \theta_b & \cos \theta_b & 0 \\ 0 & 0 & 1 \end{bmatrix} \begin{bmatrix} \cos \theta(s) & 0 & \sin \theta(s) \\ 0 & 1 & 0 \\ -\sin \theta(s) & 0 & \cos \theta(s) \end{bmatrix}, \tag{3}$$

from which the location of the *i*th actuator in cross section s can be calculated relative to the segment's proximal frame by rotating its position vector  $a_i$  from the  $\{\mathbf{e}_x, \mathbf{e}_y, \mathbf{e}_z\}(s)$  basis

of the cross section to the xyz coordinates and adding this vector to the position of the base curve at s,

$$\vec{a}_{i,xyz} = R_z(\theta_b) \begin{bmatrix} x'(s) \\ y'(s) \\ z'(s) \end{bmatrix} + R(s) \begin{bmatrix} a_{ix} \\ a_{iy} \\ 0 \end{bmatrix}. \tag{4}$$

The cross-section frames are all rotated around the y'-axis relative to the segment's proximal frame, which means the bend plane angle  $\theta_b$  also identifies a rotation from the  $\{\mathbf{e}_x, \mathbf{e}_y, \mathbf{e}_z\}$  cross-section bases into a set of  $\{\mathbf{e}_n, \mathbf{e}_b, \mathbf{e}_t\}$  normal-binormal-tangent bases for the cross sections. This property allows the strains in the actuators to be calculated by using the bend plane rotation angle  $\theta_b$  to determine the actuator positions within, and perpendicular to, the bend plane. The actuator position vectors are first rotated into the  $\{\mathbf{e}_n, \mathbf{e}_b, \mathbf{e}_t\}$  bases,

$$\begin{bmatrix} a'_{in} \\ a'_{ib} \\ 0 \end{bmatrix} = R_z^{-1}(\theta_b) \begin{bmatrix} a_{ix} \\ a_{iy} \\ 0 \end{bmatrix}.$$
 (5)

The normal component of this actuator position,  $a'_{in}$ , describes the distance between the base curve and the actuator in the bend plane. Invoking the constraint that cross-sections remain rigid, the velocity of a frame moving along the curve at unit s-velocity with a lateral offset from the base curve of  $a'_{in}$  is

$$\begin{bmatrix} \lambda_i(s) \\ 0 \\ \kappa_{s,i}(s) \end{bmatrix} = \begin{bmatrix} 1 & 0 & -a'_{in} \\ 0 & 1 & 0 \\ 0 & 0 & 1 \end{bmatrix} \begin{bmatrix} \lambda(s) \\ 0 \\ \kappa_s(s) \end{bmatrix}, \tag{6}$$

which resolves to an actuator strain of

$$\lambda_i(s) = \lambda_c(s) - a'_{in}\kappa_s(s). \tag{7}$$

Finally, the strain in the actuator can be recovered by subtracting 1 from the stretch,

$$\epsilon_i(s) = \lambda_i(s) - 1. \tag{8}$$

Internal reactions. The arm segment's internal reactions must be equilibrium with the external loads at every point along s. A general load Q is limited to twist-free loads entirely within the bend plane, but it can consist of combination of an in-plane bending moment  $Q_m$  and force  $Q_f$ . The internal reaction forces,  $q_t(s)$ , and moments,  $q_m(s)$ , are determined along the base curve, within the  $\hat{e}_t - \hat{e}_n$  coordinate system (Figure 3(b), (c)).

The base curve's tangent vector in the normal-binormal-tangent bases is given by

$$\hat{e}_t(s) = (\cos \theta(s), \sin \theta(s)), \tag{9}$$

where  $\theta$  is the tangent angle of the base curve and is found using Equation 2. The tangential force balance is

$$\mathbf{Q}_f \cdot \hat{e}_t(s) + q_t(s) = 0. \tag{10}$$

The reaction force's normal component,  $q_n(s)$ , is shown in Figure 3(c), but it is neglected in this formulation; Euler-Bernoulli beam theory assumes infinite shear stiffness and therefore a shear force does not change the predicted deformation. The moment balance is

$$\boldsymbol{r_m} \times \boldsymbol{Q_f} + q_m(s) + Q_m = 0, \tag{11}$$

where  $r_m$  is the lever arm from the point of interest to the loading point, given by

$$\mathbf{r}_{m}(s) = (z'_{c}(L) - z'(s), x'_{c}(L) - x'(s)). \tag{12}$$

Equations 10-12 demonstrate the process of finding reaction forces and moments for a tip load. Reaction forces caused by distributed loads can be found using a similar process, by expanding Equations 10 and 11 to include the additional loads. Point loads not at the tip can similarly be accommodated by modifying the lever arm  $r_m$  distance in Equation 12 to the location of the load. The internal reactions  $q_t$  and  $q_m$  from multiple discrete load cases (e.g., a tip load and a distributed gravity load) can be calculated independently, given an arm configuration, and summed. Solved displacements from discrete load cases, however, can not be superimposed. Superposition of displacements is allowed in small deformation Euler-Bernoulli beam theory, but large deformations are expected when modeling soft arms.

Cross section equilibrium. A segment's internal reaction forces are produced by the aggregate of the actuator forces. The actuators are modeled as discrete point loads and their total force is summed at each point along s. The tangential actuator force is

$$q_t(s) = \sum_{i=1}^{i=N} F_i(\varepsilon(s), P_i), \tag{13}$$

where i indicates the contribution from the  $i^{th}$  actuator. The actuator moment sum, within the bend plane and taken about the base curve, is

$$q_m(s) = \sum_{i=1}^{i=N} F_i(\varepsilon(s), P_i) \vec{a}_i \cdot \hat{e}_n, \tag{14}$$

where  $\vec{a}_i \cdot \hat{e}_n$  is equivalent to  $a'_{in}$  in Equation 5. An additional equilibrium equation is required to fully define the system. Load cases are limited to those that occur within the bend plane, and the arm is assumed to bend in a single plane. There is no internal reaction in the perpendicular plane, and the moments from each actuator must sum to zero. The second moment balance, taken perpendicular to the bend plane, is

$$\sum_{i=1}^{i=N} F_i(\varepsilon(0), P_i) \vec{a}_i \cdot \hat{e}_b = 0, \tag{15}$$

where  $\vec{a}_i \cdot \hat{e}_b$  is equivalent to  $a'_{ib}$  from Equation 5. This second moment balance is not a function of s, because the arm is assumed to bend in one plane, and is selected to be evaluated at s = 0. The perpendicular plane moment balance may not be zero at other points along the backbone, but this residual is neglected by the single-bend-plane assumption. The validity of this assumption is verified during spatial arm testing (Section 4.4).

The model is solved numerically by discretizing the simulated arm into j sections, and driving residuals of the three equilibrium equations (Equations (13), (14) and (15)) to zero. Validation efforts solved the segment model in MATLAB with fsolve.

# 3.2. Actuator characterization

The segment model simplifies actuators to uniaxial elements and defines their input state as uniaxial strain,  $\varepsilon$ , and pressure, P. The output state is force, F. An actuator force characterization  $F(\varepsilon, P)$  that covers all feasible strain-pressure combinations is required to solve.

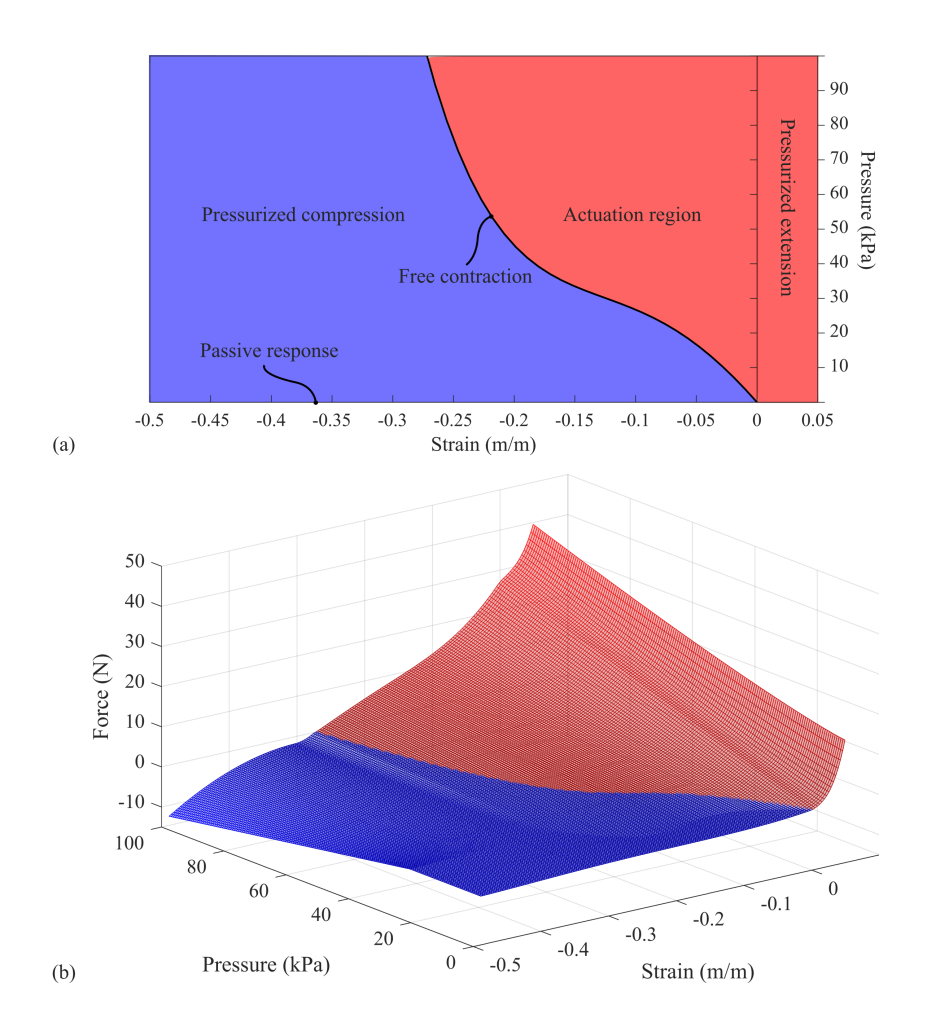


Figure 4: The actuator force characterization. (a) The strain-pressure region for a McKibben actuator. McKibben actuators have a tensile reaction force in actuation region (contraction under pressure) and the pressurized extension region (externally forced extension under pressure), which is shown as red. Pressurized compression has a compressive reaction force, which is shown as blue. (b) The empirical force function for the actuators used in the validation effort.

Each actuator in a soft arm performs the dual role of primary mover and support structure. Unpressurized actuators provide passive support. Pressurized actuators can induce deformation, but they can also be pushed or pulled beyond the actuator's stroke limits by internal loads. The segment model requires that the actuator characterization be able to predict the force for all probable combinations of strain and pressure, in order to replace a material constitutive relation.

The strain-pressure input space for a McKibben actuator can be divided into three

regions (Figure 4): actuation, pressurized compression and pressurized extension. McKibben actuators contract when pressurized, and their actuation region is defined as the region in which they produce a tensile force at a contraction strain. Actuation and pressurized compression are divided by the free contraction line,  $P(\varepsilon_{FC})$ . The actuator produces zero force along this line, and the line represents the pressure required to overcome the energy spent deforming the elastomeric tube and plastic sheath. Pressurized compression occurs when the pressure is insufficient to provide that energy at a given strain. The actuation and pressurized extension regions are separated by the zero strain line. Pressurized extension can only occur if the actuator is subjected to an opposing load higher than the blocked force (force at zero strain for a given pressure). Passive extension and compression lie along the base of the pressurized regions.

An actuator characterization can be formed by modeling each region, but the segment model requires that the characterization be continuous at the region boundaries. Physical models, while more likely to generalize across actuator designs, focus on capturing core mechanics, and because the core mechanics vary from region to region, simple physical models are unlikely to match at region boundaries. This article uses empirical characterizations with forms selected to guarantee consistency at region boundaries [33]. These characterizations were developed from force-pressure-strain data collected in each region and are not extrapolated beyond the tested strains and pressures. The empirical force function is plotted for the strain-pressure space in Figure 4. The fit forms, coefficients and testing details are discussed in Appendix A.

#### 3.3. Segment model special cases

There are three segment model simplifications of note: (1) the planar case, (2) constant curvature and (3) structurally minimal unloaded arms. First, the segment model is simplified in the planar case (where actuators lie in one plane) by noting that the bend angle  $\theta_b = C \equiv 0$  regardless of actuator pressurized. An arm with only two actuators in each segment is inherently planar. An arm with more actuators can act as a planar arm by pressurizing actuators in groups. The planar validation arms have four actuators per segment, grouped

in two sets, with one set on each side of the segment (Figure 2). Each group is pressurized together. Planar arms are studied extensively in this manuscript because they demonstrate many of the same mechanics as spatial arms in a more controllable setting.

Second, the segment model reduces to a constant curvature model when the arm is under negligible external load. The arm may be self-stressed, caused by pressurized actuators acting on unpressurized actuators, but the absence of external loads means that the sum of the internal reaction forces and moments (Equations (13)-(15)) are identical and zero along s. If the arm cross section and actuator are also identical along s, the constraining equations predict the same curvature and base curve stretch (or neutral axis height) at every point.

Third, the segment model can be further simplified for unloaded planar arms with two actuators and unloaded spatial arms with three actuators. These arms are termed structurally minimal in this manuscript, which means that they contain the minimal number of actuators required to access their maximum degrees of freedom. Structurally minimal arms have a sufficiently simple strain state to allow a closed form solution. Consider a planar arm with two actuators separated by a distance 2R. The arm is under no load, which reduces the model to two equilibrium equations that are identical along s:

$$F_1 + F_2 = 0, (16)$$

$$F_1 R - F_2 R = 0. (17)$$

Regardless of pressure in either actuator, the only solution to Equations (16) and (17) is

$$F_1 = F_2 = 0. (18)$$

The free contraction line is the only location in the actuator's strain-pressure space with zero force (the line is labeled in Figure 4(a)). Along this line, all pressure work is used to deform the actuator, which results in the maximum contraction possible for a given pressure. The contraction strain increases monotonically with pressure and is given by  $\varepsilon_{FC} = \varepsilon_{FC}(P)$ , where  $\varepsilon_{FC}$  is positive in extension and negative in contraction.  $\varepsilon_{FC}(P)$  may be found by inverting the free contraction line fit  $P(\varepsilon_{FC})$  or, if used only in the special cases, by refitting the characterization data with pressure as the independent variable. Satisfying Equation

(18) requires that each pressurized actuator be contracted maximally and each unpressurized actuator have zero strain. If only one actuator is pressurized, the arm bends in the direction of that actuator, while the opposing actuator is unstrained, which gives a neutral axis height of

$$h = -R. (19)$$

The unpressurized actuator experiences no length change, while the pressurized actuator contracts maximally to  $\varepsilon_{FC}(P)$ . The stretch changes linearly through the cross section, which gives a base curve stretch of

$$\lambda_c = 1 + \frac{\varepsilon_{FC}(P)}{2}. (20)$$

The base curve's curvature is

$$\kappa_c = \frac{-\varepsilon_{FC}(P)}{(2 + \varepsilon_{FC}(P))R},\tag{21}$$

which is calculated by solving Equation (7) for the actuator along the neutral axis, where i = 1 and  $a'_{in} = -R$ . Planar arms with n actuators pressurized together on each side do not change the model's solution. Each force F is replaced by nF and the coefficient n cancels.

Unloaded spatial arms composed of three actuators are also structurally minimal, and the methodology used in the planar case can applied. Let each actuator be at distance  $\vec{a}_i$  from the cross section center (Figure 3(d)). Without loss of generality, assume the bend direction is such that Actuator 1 and 2 lie above the base curve and Actuator 3 lies below it. The force and moment equilibrium relations from Equations (13)-(15) become

$$F_1 + F_2 + F_3 = 0, (22)$$

$$F_1 \vec{a}_1 \cdot \hat{n} + F_2 \vec{a}_2 \cdot \hat{n} + F_3 \vec{a}_3 \cdot \hat{n} = 0, \tag{23}$$

$$F_1 \vec{a}_1 \cdot \hat{b} + F_2 \vec{a}_2 \cdot \hat{b} + F_3 \vec{a}_3 \cdot \hat{b} = 0.$$
 (24)

It can be shown through substitution, assuming no actuator lies on top of another and the actuators are not all in one line, that

$$F_1 = F_2 = F_3 = 0, (25)$$

regardless of exact arrangement. The only possible solution is for each pressurized actuator to be contracted maximally and each unpressurized actuator to have zero strain.

The neutral axis height and bend direction for the three actuator segment can be determined geometrically given that the strain in each actuator,  $\varepsilon_i$ , is determined by the free contraction line  $\varepsilon_{FC}(P_i)$ . Assuming two actuators are pressurized, the neutral axis lies along the unpressurized actuator, which must be on the opposite side of the arm as the curvature direction. The neutral axis location for three actuators equally spaced around a circle with radius R, of which Actuator 1 and 3 are pressurized, is

$$h = \vec{a}_2 \cdot \hat{e}_n,\tag{26}$$

where  $\hat{e}_n = (\cos \theta_b, \sin \theta_b)$ . The bend direction must lie between the two actuators. If Actuator 1 and 3 are pressurized, the bend direction is

$$\theta_b = \tan^{-1} \left[ \sqrt{3} \frac{\varepsilon_{FC}(P_1) + \varepsilon_{FC}(P_3)}{\varepsilon_{FC}(P_1) - \varepsilon_{FC}(P_3)} \right] - \frac{\pi}{3}. \tag{27}$$

The neutral axis curvature  $\kappa_{NA}$  is

$$\kappa = \frac{-\varepsilon_{FC}(P_1)}{\vec{a}_1 \cdot \hat{e}_n - \vec{a}_2 \cdot \hat{e}_n},\tag{28}$$

and the base curve's curvature can be calculated using Equation (7), by noting that  $\lambda_2 = 1$  and  $\lambda_1 = 1 - \varepsilon_{FC}(P_1)$ . Despite actuator complexity and arm nonlinearity, bend curvature and direction can be calculated explicitly. Spatial arms with more than three actuators do not follow this closed form solution, because the actuator resultant forces are not necessarily identical and zero.

# 4. Model Validation and Analysis

This section validates the model for planar and spatial arms. The model was validated for five single segment planar arms (with widths of 20 mm, 30 mm, 40 mm, 50 mm and 60 mm), a two segment planar arm and a single segment spatial arm.

# 4.1. Validation test methods

Planar and spatial arms were tested by applying a constant load while pressurizing selected actuators. Actuator pressures were measured using Honeywell TruStability 30 PSI (200 kPa) pressure sensors, which have a resolution of 0.2 kPa and an accuracy of  $\pm 0.55$  kPa. Each arm's deformed state was measured throughout the experiment with an OptiTrack motion capture system. Planar arms had two OptiTrack markers mounted on each plate, directly above the actuators, in order to capture the plate's position and orientation (Figure 5(a)). Spatial arms had three markers mounted on the base plate and two markers mounted on all other plates (Figure 5(b)).

Loads were applied to arms by connected weights to the arm tips via string. Planar arms

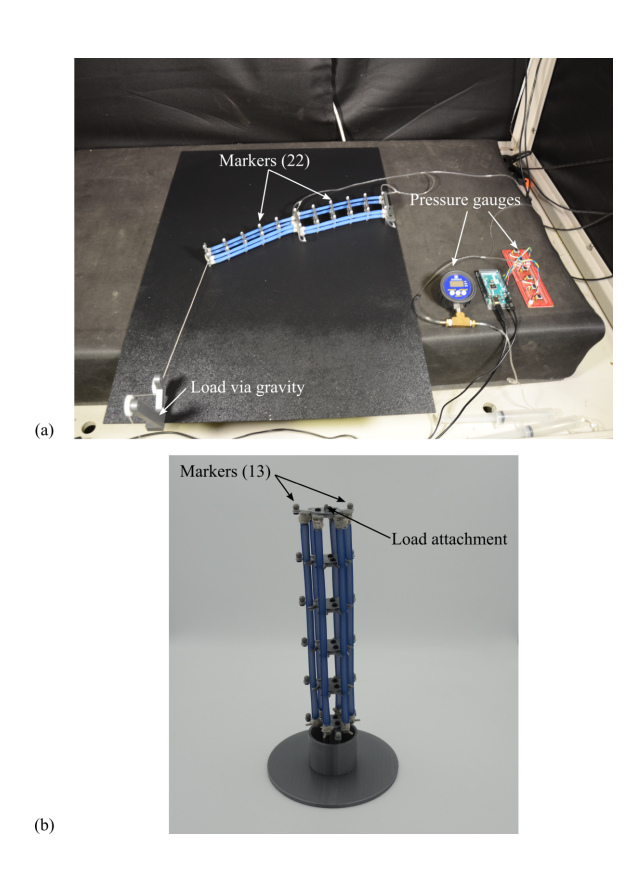


Figure 5: Validation experiments. (a) The planar arm test set-up, shown with a multisegment planar arm. A suspended weight was connected to the arm tip via a line run over a pulley. (b) Markers and the load attachment point for a spatial arm. There were two lines of six OptiTrack markers separated by 120° and an additional marker at the base.

load lines were run under a pulley that was vertically aligned with the arm tip, and over a second, higher, pulley. The weight at the end of the line was suspended against gravity, which provided a constant force throughout the experiment. The planar test platform was lubricated with WD-40 prior to testing. Spatial arms were tested upright, with lines short enough to not touch the test platform during testing.

# 4.2. Planar single segment validation

The planar single segment validation tests were conducted on segments with widths of 20 mm, 30 mm, 40 mm, 50 mm and 60 mm. Each segment was otherwise nominally identical and conformed to the design presented in Section 2. Segments were tested at loads ranging from 0 N to 1.57 N, depending on segment width. The planar model was solved for selected cases with a tip force magnitude  $|Q_f|$  equal to the experimental force, and the moment  $Q_m = 0$ . The load's direction vector changes slightly as the load is lifted and the arm tip moves, which was included in the model by defining the  $Q_f$  vector to be from the arm tip to the pulley. Figure 6 compares the model and experiment for five widths and three forces (45 cases total). Three pressures are compared within each force-width case.

Three trends between design variables and segment behavior are apparent from the results displayed in Figure 6. First, the load-free range of motion decreases as segment width increases (see the first column of Figure 6). Equation (21), the model's planar load-free special case, matches this trend and predicts an inverse relationship between segment width and curvature for equivalent actuator strains. Second, the passive stiffness increases with segment width. Consider the 0 kPa comparisons in the second column of Figure 6. Each segment was unpressurized and subjected to the same force, but smaller widths were deflected further. Third, the arm's ability to resist loads increases with width. The labeled forces in the third row of Figure 6 were the loads that caused a deflection of approximately -5 cm from the arm's initial midline, at a pressure of 80 kPa. The force the segments can resist increases monotonically with width.

The model's accuracy was quantified with an average distance error (Table 1). The error metric is an average of the distance between the model prediction and the experiment at

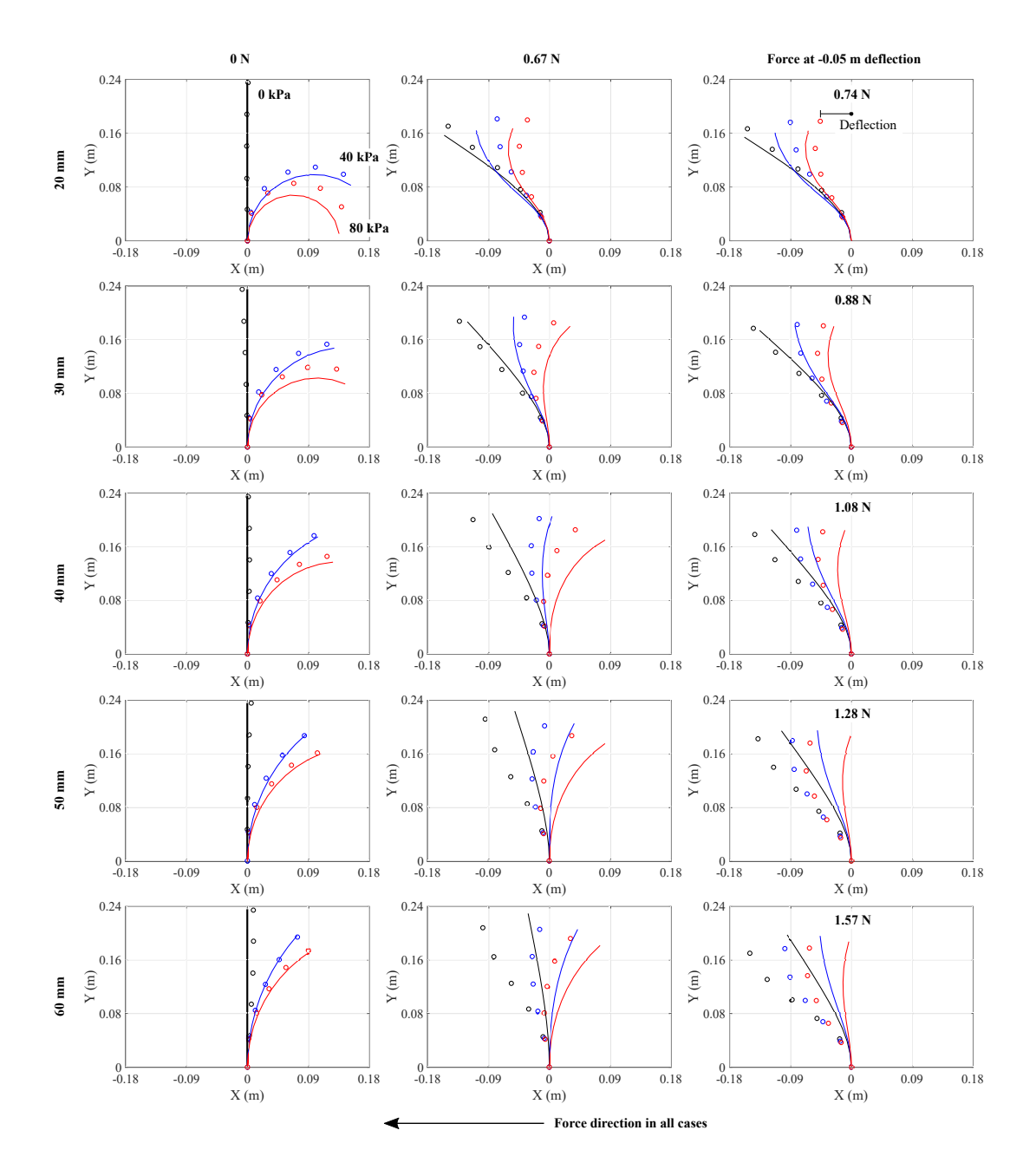


Figure 6: Comparison of experimentally measured arm centerline (dotted lines) and model results (solid lines) for five widths and three loads. Single segment planar arms were loaded at their tips, pulled left and pressurized to bend right while under load. Experimental results are the average of at least three trials. Each force-width case compares three pressures: 0 kPa (black), 40 kPa (blue) and 80 kPa (red). Segment width increases top to bottom and is given by the labels at the left of each row. The force applied increases left to right and is given by the labels at the top of each column. The first two columns have a constant force, while the third row is the force to achieve an approximately -5 cm deflection from the midline. The force values for the third column are given within each force-width case plot.

Table 1: Whole length average distance error (mm) for planar segments.

Force	20 mm	30 mm	40 mm	50 mm	60 mm
0 N	10.6	8.1	4.2	3.2	3.3
0.67 N	11.0	9.4	17.3	26.6	29.1
Highest	9.6	8.0	16.1	28.1	33.1

Table 2: Average tip distance error (mm) for planar segments.

Force	20 mm	30 mm	40 mm	50 mm	60 mm
0 N	20.4	6.6	4.2	4.5	5.0
0.67 N	17.6	32.0	46.7	26.6	57.1
Highest	9.7	25.3	46.0	28.1	58.7

six points evenly spaced along the segment length, for the three pressures compared within a force-width case. The distance error naturally increases along the length, because the arm behaves like a kinematic chain. Small differences in curvatures can magnify position differences down the length, and the highest error is expected at the tip. Table 2 presents the same average distance error computed only for the segment tips, which is the equivalent to end effector error.

Three additional sources of model error are worth note: friction, an observed hysteresis and the neglected arm shear stiffness and actuator bending stiffness. All planar single segment simulations were solved without including friction between the test platform and the arm. The error caused by friction is most visible in the first column of Figure 6, where the arm is modeled as load-free but experiences some friction. The difference between the model and the experiment is a combination of friction and unmodeled bending stiffness, and both factors affect the narrowest arms the most, which reach the highest curvatures and produce the least force. The total error establishes a maximum error due to friction, and in the narrowest arm tested (20 mm), the maximum tip error is 20 mm.

The second source of error is an observed hysteresis in the pressure-position response. Validation tests were conducted by pressurizing from 0 kPa to approximately 90 kPa, at least three times for each force-width case, and the arm's deformed state was recorded during inflation and deflation. Figure 6 compares the model to the average centerline position, while Figure 7 plots the range of measured states for the 20 mm, 40 mm and 60 mm segments when subjected to a 0.67 N tip load. The range is most varied at 40 kPa in every case, and measurements were noted to cluster near the two extremes: the left-most state came from inflation and the right-most state came from deflation.

The observed lag between the pressure input and deformation may be a hysteresis caused by a combination of internal (material) and external friction, but it may also be a dynamic phenomenon. The model is quasi-static, but motion of the physical arm requires an acceleration, induced by the force imbalance from pressurization. Arm force, and thus acceleration, is low at low pressures and at high strains, which occur at the start and end of the tested motions. The inflation and deflation rate may exceed these accelerations, creating a lag at the motion's start. External friction and material damping dissipate momentum, which may eliminate the lag at the motion's end. The quasi-static and hysteresis-free assumptions simplify the model and decrease solution time, but predicting the observed lag would require that the model be extend to include hysteresis and dynamic effects. The range of results is small at high and low pressures, verifying that the model is suitable for predicting arm capabilities that are not affected by the mid-motion variance (e.g., maximum reach with a load applied).

The third source of potential error is the actuator's bending and shear stiffnesses, which are assumed to be zero and infinite, respectively. The actuators are highly compliant, and their bending stiffness is low, but at high pressures and curvatures the unmodeled bending stiffness is a likely cause of error. Thin arms that reach high curvatures are most affected (e.g., the 20 mm arm under no load in Figure 6). An effective bending stiffness can be included in an Euler-Bernoulli model, but that stiffness must be characterized across the actuator's strain-pressure domain.

Euler-Bernoulli beam theory neglects shearing deformations by assuming that the cross section is planar and perpendicular to the arm's base curve. Physical soft arms can shear, which causes the model to overpredict arm reach under high loads. The increasing model

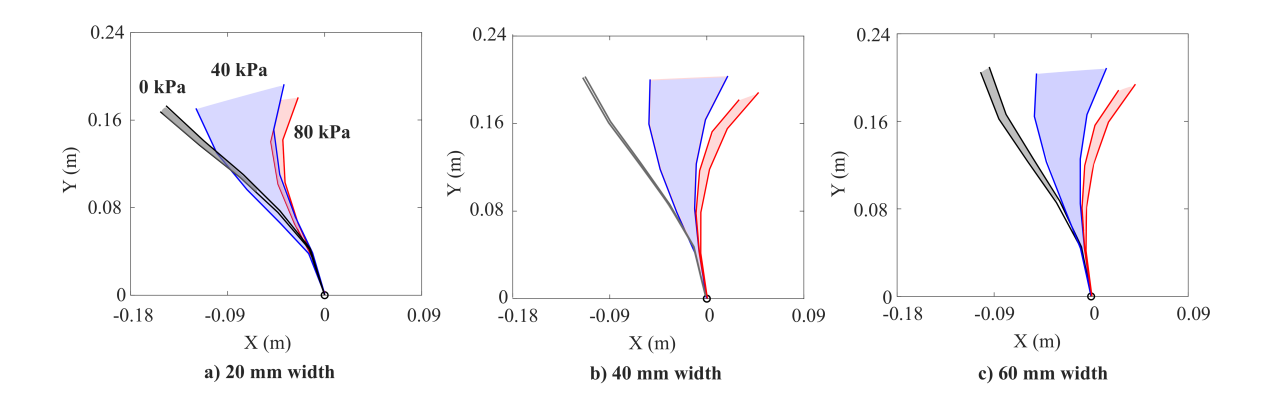


Figure 7: Variation in arm segment position for three force-width cases. The force applied in each case is 0.67 N, and results are plotted for widths of (a) 20 mm, (b) 40 mm and (c) 60 mm. Each plot contains the outermost measurements (left and right) for three given pressures. Measurements for each case were drawn from at least three trials, and data was collected during inflation and deflation.

error, as load and width increase, is attributed predominantly to neglected shearing deformations. The second column of Figure 6 demonstrates the affect of width on shearing and bending deformations, given the same number and arrangement of actuators. The arm's shear stiffness is similar across widths, because the amount of material in the arm is independent of width, while the bending stiffness increases with actuator separation. Larger widths bend less, and the load case is closer to a pure shear. Shear error is a fundamental limitation of Euler-Bernoulli beam models, and the segment model overestimates stiffness of shear-affected arms (see comparisons of the 60 mm arm in Figure 6). Wider arms are not universally shear-affected; the likely shear error increases when the shear stiffness is low compared to the shear load, and wider arms with more actuators are expected to have lower shear errors.

Other beam and rod models can include shear (e.g., Timoshenko beam theory). Although models with shear are more complex to formulate and solve, the more significant limitation is that they require actuator characterizations that predict shear stiffness as a function of strain and pressure. The shear-free model is most accurate at small widths and low loads compared to the arm's shear stiffness, and it is least accurate when wide arms are subjected to high loads (Figure 6).

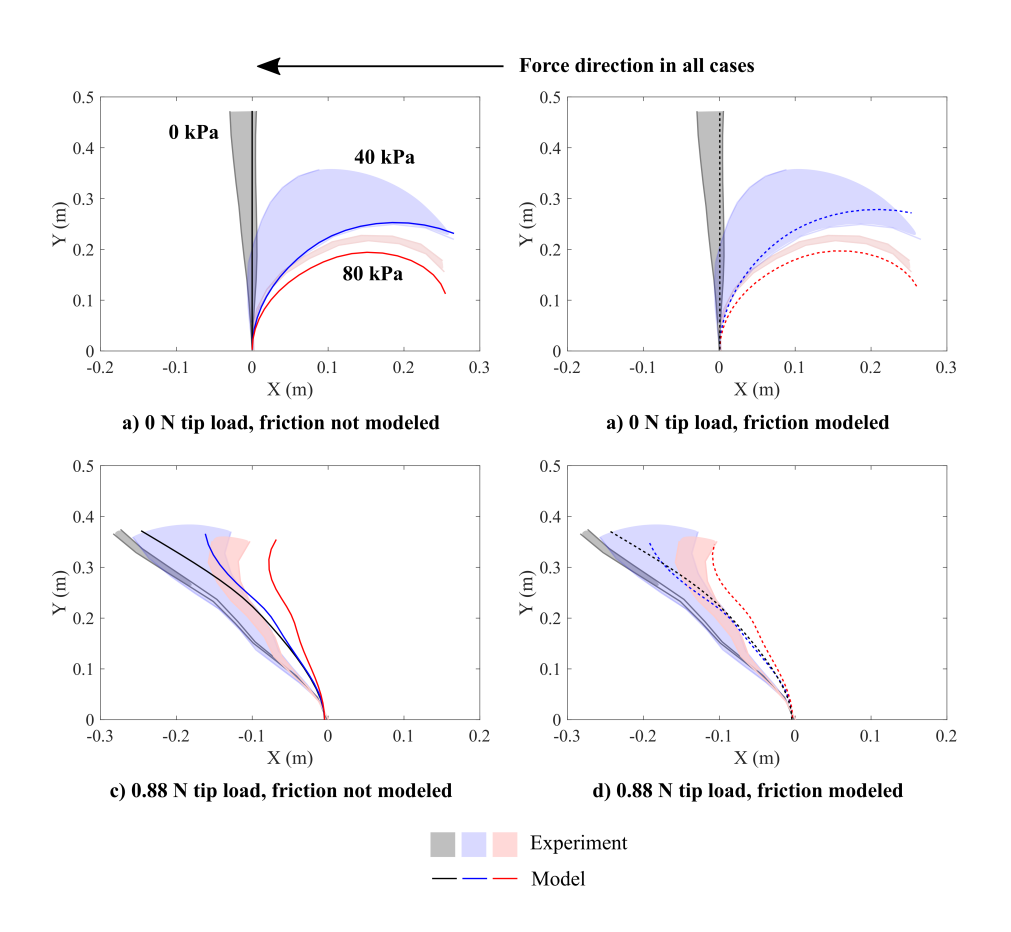


Figure 8: Comparison of model (solid lines) and experiment (shaded regions) for a two segment planar soft arm at pressures of 0 kPa (gray), 40 kPa (blue) and 80 kPa (red). A leftward tip load was applied to the arm, and both arm segments were pressurized to bend right. Each shaded region represents the range of measured arm shapes for that pressure, taken from at least four trials. Deformed shape was measured during inflation and deflation to capture the dynamic range. (a) The arm was load free, and modeled without friction. (b) The arm was load free, but the model was computed with a friction load. (c) The arm was subjected to a 0.88 N tip load and modeled with the tip load but no friction. (d) The arm was subjected to a 0.88 N tip load and modeled with the tip load and a friction load.

# 4.3. Planar multisegment validation

The model was validated on one planar arm with two segments (Figure 2). The 60 mm (base) and 30 mm (tip) wide single segments were combined to form an arm 0.47 m long. The arm was tested in the same set-up as the planar single segments, with a modified load placement to keep the load approximately perpendicular to the arm's initial centerline. Both segments were pressurized equally and in the direction opposing the load. Figure 8(a) and

(c) compare measured and predicted deformed shape for the arm with no tip load and a 0.88 N tip load. The expected shape is captured, though the tip error is visibly higher when loaded. The longer arm's higher tip error is expected, because the length increases the total friction and the accumulated shear angle error.

The deformed shape was also compared to a model prediction that included friction, in order to evaluate how much tip error may be caused by friction. Sliding friction is inherently related to velocity, and is not straightforward to include in a quasi-static model. A first order estimate of friction was obtained by aggregating the friction moment along an initially straight arm and applying an equivalent tip load. The friction torque can be estimated by

$$T_{fric} = \int_0^L \mu \frac{mg}{L} \ell d\ell, \tag{29}$$

which results in an equivalent force of

$$F_{equiv.} = \frac{\mu mg}{2}. (30)$$

The model only applies when the force the arm can apply at a particular point is higher than the friction force, because motion is required to encounter friction. The arm had a mass of 120 g and the friction coefficient was selected as  $\mu=0.3$  based on accepted values for sliding plastic. Figure 8(b) and (d) compare the model results when friction is included. The model without friction had an error of 61.5 mm from the averaged measured tip position at 80 kPa with a 0.88 N tip load. That error dropped to 24.2 mm when friction was modeled.

# 4.4. Spatial single segment validation

The spatial form of the model was validated on a 40 mm diameter single segment spatial arm (Figure 1). Spatial arms can be operated by pressurizing a single actuator, with a discrete number of possible directions, or by pressurizing two actuators simultaneously, which lets the arm bend in any direction. Direction is controlled through actuator selection and the proportion of pressure in each actuator. The model was validated with single and dual actuator tests, with and without a tip load.

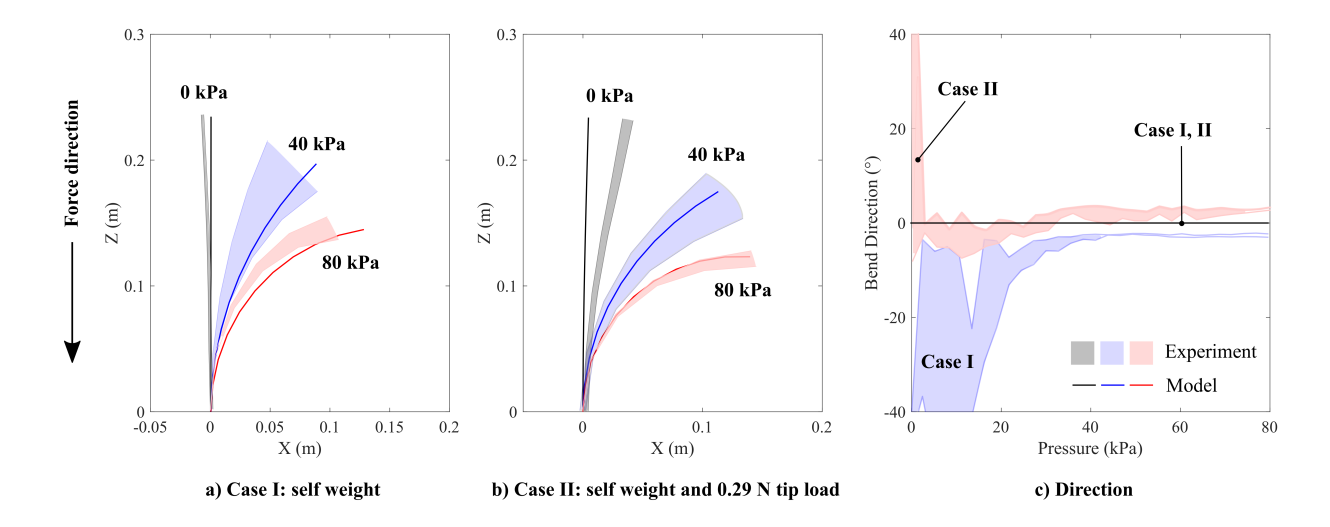


Figure 9: Comparison of the model (solid lines) and experiment (shaded regions) for a spatial arm with one actuator pressurized. A downward tip load was applied to the arm, and one actuator was pressurized. Experimental results are plotted as a range, extracted from at least four trials. (a) Arm shape comparison for Case I: No tip load is applied, but the arm is loaded with its own weight. (b) Arm shape comparison for Case II: A tip load of 0.29 N is applied downward, along the gravity vector. The arm is additionally loaded with its own weight. (c) Bend direction comparison for Case I and II, plotted in degrees. Actuator 1 is pressurized in both cases. The model-predicted direction for Case I and II are identical and zero. Colors in (c) indicate Case I or II, not specific pressures.

The spatial arm was tested vertically and upright. Tests with loads applied had a 30 g suspended mass connected to the arm tip, which is equivalent to a 0.29 N tip load directed downward. The model prediction also included a distributed gravity load from the arm's 62 g mass, which was applied evenly over its 0.235 m length. Figure 9 compares the experimental result and model prediction for single actuator use. Actuator 1 was pressurized in all cases (see Figure 3 for actuator numbering).

Model shape error was quantified with the same distance metric as the planar segments and is given in Table 3. The errors were, in general, lower than the planar comparisons, which is likely due to the lack of friction and reduced shear from the lower loads. The relatively high error at 0 kPa is most likely due to the arm's low stiffness when unpressurized, which means the physical arm is most sensitive to bending and neglected shearing deformations under and off-center load. There are multiple numerically-viable equilibrium points for a

Table 3: Average distance error (mm) for spatial arm.

	Tip,	Tip,	$\mathbf{Arm}$	Arm,
Pressure	0 N	0.29 N	0 N	0.29 N
0 kPa	7.9	31.0	3.1	13.0
$40~\mathrm{kPa}$	16.0	13.0	6.5	5.5
80 kPa	25.0	4.3	11.0	2.2

downward load on an unpressurized arm: pure compression or through a combination of compression and bending, by assuming the load is not initially aligned with the arm center. The deformation in the second case underpredicted because shear is excluded. The pure compression equilibrium requires that the downward load remain perfectly aligned with the arm's central axis, and generates only axial compression. Figure 9 shows only the combined bending and compression equilibrium point; the pure compression equilibrium point is visually close to the bending equilibrium point, and is omitted for clarity.

Two equilibrium points presents the possibility of buckling, in this case from column loading to beam bending. However, sudden deformations at critical loads were not observed during testing. Each test arm inevitably had small imperfections that imparted a slight initial curvature (on the order of 0.1 to  $1^{-1}/m$ ) and all loads, regardless of magnitude, increased this curvature.

The single-actuator bend direction prediction shown in Figure 9(c) matches the experimental results poorly for pressures under 20 kPa, but matches the experiment well for higher pressures. This discrepancy is likely caused by the physical's arms initial curvature, exacerbated by direction sensitivity in the near-straight configuration. During testing, the arm was allowed to "fall" to its preferred equilibrium. The unloaded arm had a slight initial curvature due to manufacturing imperfections that likely favored the most compliant actuator, while the loaded arm's initial direction varied more randomly. Even small deformations in the near-straight configuration can result in large changes in the bend direction. Each arm reoriented to Actuator 1's direction upon pressurization, but the intermediate measurements can be considered a dynamic event. The loaded arm reached steady state faster, but

Table 4: Evaluation of the bend plane fit quality.

Case	Load	$R^2$	RMSE (mm)	
Single actuator	0 N	0.995	0.57	
Single actuator	0.29 N	0.999	0.69	
Dual actuator	0 N	0.999	0.78	
Dual actuator	0.29 N	0.984	0.98	

a quasi-static model cannot evaluate whether the speed was caused by the load. The loaded arm had an average direction of  $0.51^{\circ}$  at steady state, and the unloaded arm had an average direction of  $-2.7^{\circ}$ , compared to the model's prediction of  $0^{\circ}$  for both.

The second set of validation tests focused on dual actuator pressurization, which can produce continuous direction change. The dual-actuator tests pressurized Actuator 1 followed by Actuator 5, but otherwise followed the same procedure as single-actuator tests. The experiment and model prediction are compared in Figure 10. The direction and pressure plots are taken from continuous actions, and the measured pressure profiles were used as model inputs. The root mean squared error between model-predicted direction and experiment was 6.3° for the case without a tip load and 17° for the case with a tip load. The angle offsets may come from manufacturing imperfections in the arm, while the larger deviations (e.g., at Index 0) are more likely to be caused by dynamic events.

The spatial validation test results were used to verify the single bend plane assumption. Bend planes were identified from the x-y coordinates of the arm's OptiTrack markers. A line was fit to each set of markers, and the bend direction was calculated from slope in the xy-plane. The single plane assumption was verified by evaluating the fits' coefficient of determination  $(R^2)$  and RSME (see Table 4). The values presented are the minimum  $R^2$  and the maximum RMSE.

## 5. Workspaces under Load

The final results section demonstrates one method of using the segment model to explore soft arm mechanics. This section analyzes the workspace of planar soft arms, which is the set

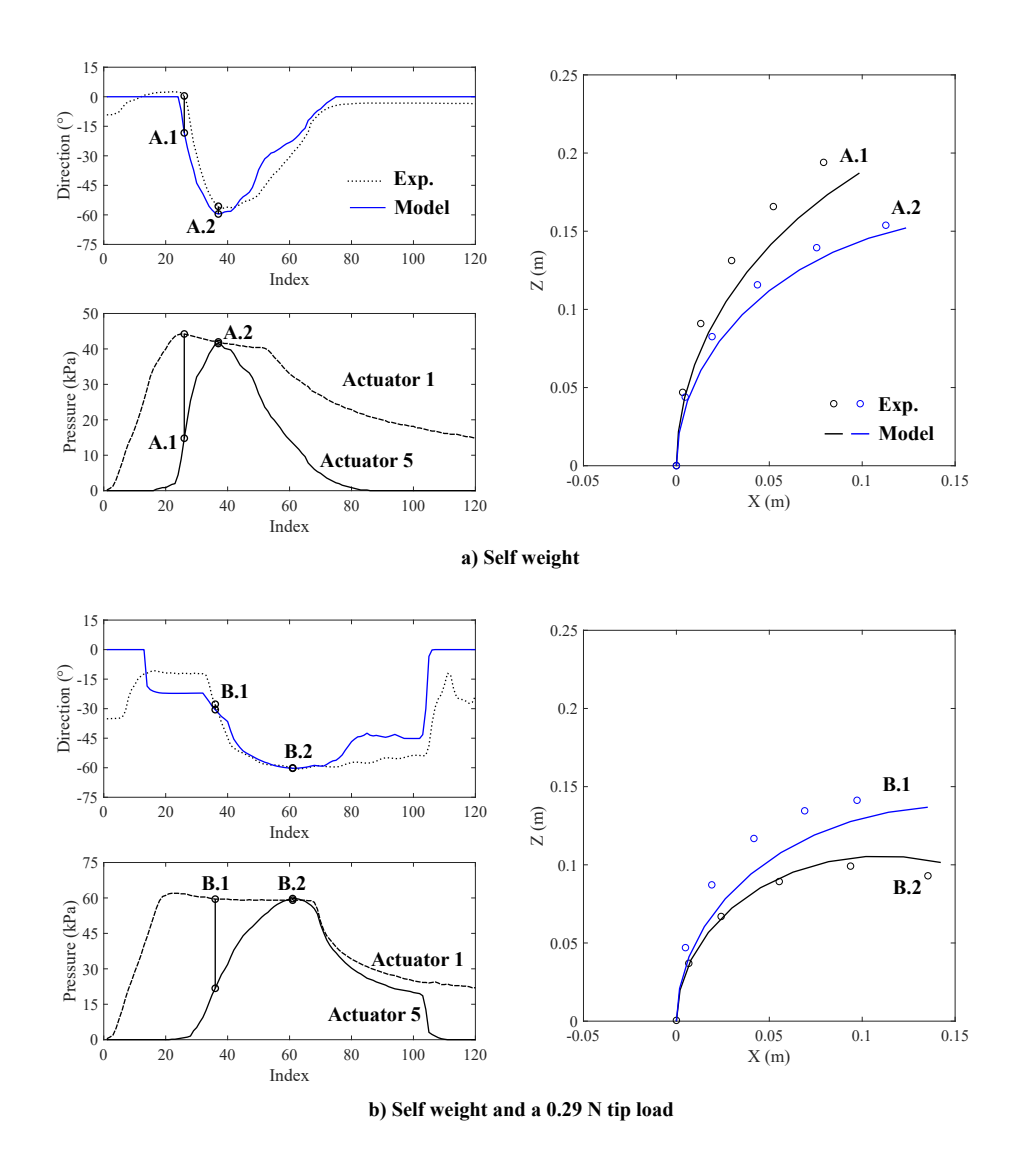


Figure 10: Comparison of the model (solid lines) and experiment (dotted lines) for a spatial arm with two actuators pressurized. Tip loads were applied downward, and two actuator were pressurized to continuously change arm direction. The plotted results were extracted from one trial. The two pressure profiles are plotted and matched to the bend direction by an index on the x-axis. Curvature results were extracted for labeled indices A1, A2, B1 and B2. (a) No tip load is applied, but the arm is loaded with its own weight. (b) The arm is loaded with its own weight and a tip load of 0.29 N is applied downward, along the gravity vector.

of reachable points. The validation results demonstrated indirectly that load and segment width change the arm's range of motion, but the segment model can analyze workspace directly.

Consider a single segment planar arm with width w that is otherwise identical in design and length to the validation planar arms. The arm is represented by a base curve, and the most commonly adopted kinematic model is a piecewise constant curvature. The segment model predicts constant curvature for unloaded arms, but the model does not support assumptions of zero stretch along the base curve – even for unloaded arm. An unloaded planar arm's neutral axis lies along the actuator opposite the bend (Equation (19)), and the resulting base curve stretch can be calculated with Equations (B.1) and (21). Figure 11(a) compares the tip paths of a 30 mm wide, unloaded planar segment with and without stretch modeled.

Let the same 30 mm planar segment be loaded perpendicular to its tip. Figure 11(b) compares the model-predicted tip path for an assisting load (positive, pulling in the direction of curvature) and an opposing load (negative, pulling against curvature). The opposing load causes the base curve to shorten more and bend less, while the assisting load causes it to bend more and shorten less. The tendency to shorten under opposing loads can be explained by considering the forces acting within the cross section. Moving an opposing load requires the pressurized actuator to exert a higher force. That higher force must be in equilibrium with the unpressurized actuators, which are compressed until their reaction force is sufficient.

Increasing the magnitude of the opposing load pulls the arm tip back to the centerline (Figure 11(c), plotted only for actuator pressures of 100 kPa). Average curvature is reduced and the effective length shortens, but the arm shape is more complex at higher loads. An arm's maximum load and maximum reach always occur at the highest achievable pressure,  $P_{max}$ , which is 100 kPa for the actuators used in validation tests. Load and reach are inversely related, and both are affected by segment width. Load and reach comparisons are complicated by arm shortening, because the set of reachable x-y positions at load F are not the set of reachable x-y positions at 2F. A comparative parameter S is defined as the arc length path, measured outward from x=0, of the set of tip positions possible at  $P_{max}$  (see Figure 11(c)). The load at each point along S is the maximum load that can be resisted at that point. Figure 11(d) plots the relationship between S and the corresponding maximum load for five segment widths. This plot represents the loaded workspace of a single segment

planar arm. Maximum load does increase with segment width, but the reach over which loads can be applied narrows. All five widths can apply a load of 0.5 N, but the 20 mm segment can apply that load out to a reach of 0.23 m, while the 60 mm segment can only

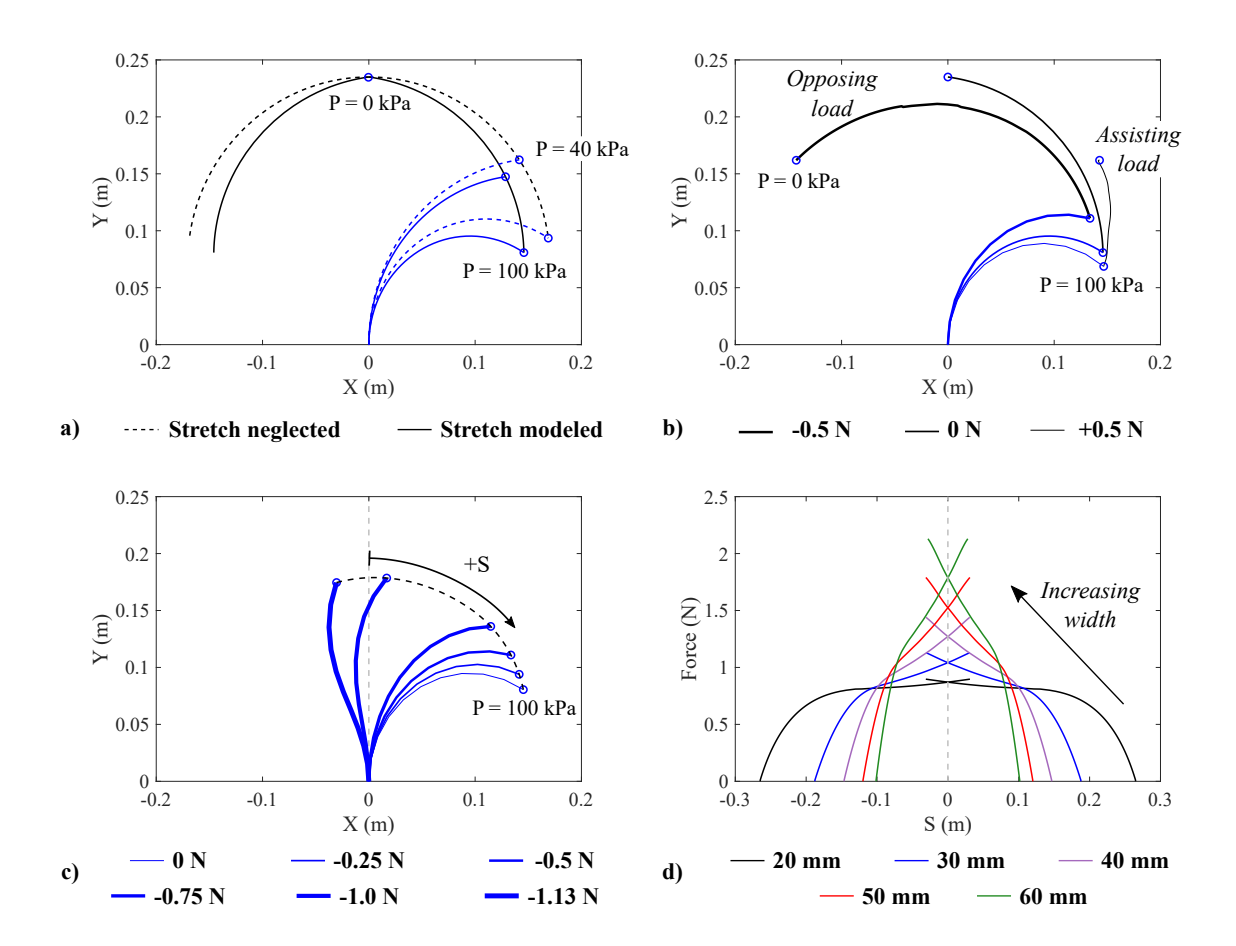


Figure 11: Model-predicted workspace of a 0.235 m long single planar segment. Blue lines in (a)-(c) are arm shapes, and blue dots are tip positions. (a) Comparison of unloaded, 30 mm wide segment's tip path if stretch (in this case, compressive) is neglected, versus the model-predicted tip path, which includes stretch. The path was computed for pressures from 0 to 100 kPa in either the left or right actuator. (b) Comparison of the model-predicted path for a loaded segment with an assisting load (positive) and an opposing load (negative). Loads were applied left and perpendicular to the segment tip and the right actuator was pressurized. (c) Comparison of deformed shapes for a 30 mm wide segment with opposing loads applied left and perpendicular to the segment tip. The right actuator was pressurized to 100 kPa. (d) Maximum load a segment with a particular width may hold at a point S along its tip path (defined in (c)). Results are mirrored left and right, representing pressurizing either the left or right actuator.

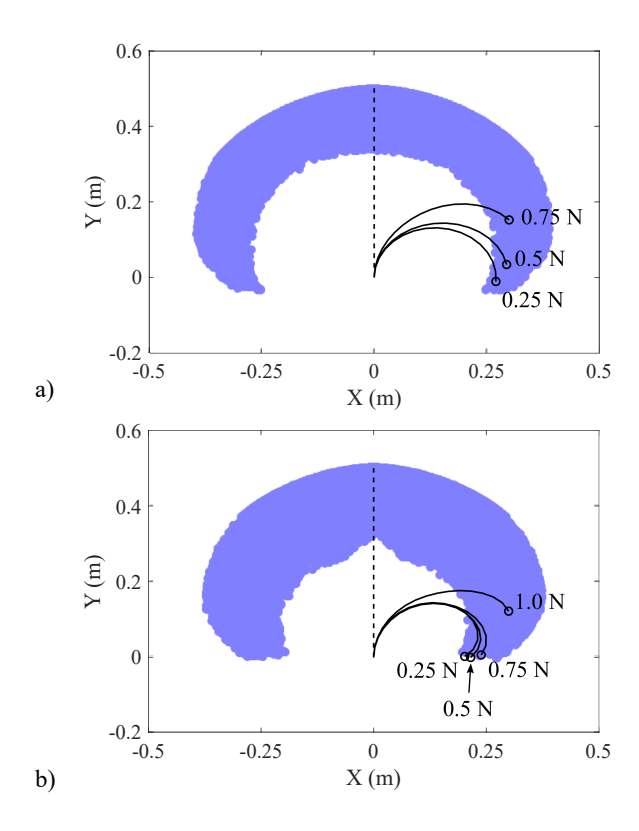


Figure 12: The workspaces of multisegment soft arms in obstacle free environments. The analyzed arms have four segments, each of which is 0.125 m long. The shaded regions represent the unloaded workspace, while the lines are deflected arm shapes for the labeled loads, assuming maximum pressure in each actuator. (a) Results for a constant-cross-section arm, with a width of 40!mm. (b) Results for a tapered-cross-section arm, with widths of 50 mm-40mm-30mm-20mm from base to tip.

## apply it out to 0.09 m.

Increasing the number of segments in an arm changes the workspace from a line to a two dimensional region. The shaded region in Figure 12(a) shows the workspace of an unloaded soft arm with four segments. The analyzed arm had a constant, 40 mm wide, cross section, with four actuators in each segment and a total length of 0.5 m. The workspace was generated by solving the model for 10000 sets of random actuation pressures, assuming  $P_{max} = 100$  kPa. Figure 12(a) also plots the tip location for the maximally actuated arm under opposing loads applied perpendicular to the arm tip. Each line represents the maximum extent of the arm's reach while carrying that load, and the behavior follows the trend established in Figure 11(d).

The practical implications of the results in Figure 11 and 12 is that, first, the extremes of the reachable space (the pointed tips in Figure 12) are least suited to forceful manipulation, and, second, that load capacities are directional. Consider an opposing load that starts at the workspace centerline and is carried left or right. The higher the load's magnitude, the shorter the distance the arm can move the load. The unloaded workspace edges have no load capacity, which means that actions such as reaching left, contacting an object partway through the workspace and pushing it to the edge of the unloaded workspace are not possible. However, load capacity is directional. An arm bent left to its maximum reach has a high load capacity when moving right. If the same opposing load starts on the opposite side of the workspace (e.g., if moving left, it starts in the right quadrant), the arm can move the object across the workspace centerline and into the adjacent quadrant, resulting in a much longer stroke. Stroke direction and soft arm placement relative to the load must be considered in order to maximize an arm's ability to perform a given task. This large variation in loaded workspace size is fundamental to the soft arms studied in this manuscript, and is inherently different from jointed, motor driven robot arms.

The same analysis was repeated for a tapered arm (Figure 12(b)). The analyzed arm had the same length, number of segments and number of actuators, but the segments had widths of 50 mm, 40 mm, 30 mm and 20 mm, from the base to the tip. The internal moment in tip-loaded arms is highest at the base and zero at the tip. Tapered arms more closely match this profile, and have the most geometric stiffness where the moment is highest. The tapered arm's unloaded workspace is larger than the workspace of the constant-cross-section arm, and the tapered arm resists higher loads. However, the fundamental arm behavior is unchanged, and the extremes of the workspace are still significantly weaker than areas near the midline.

## 6. Conclusion

Soft robotics currently lacks quantitative design guidance and specific tools for simulationbased design. Designs are improved through iterative prototypes, qualitative analysis and intuition, which is a time-consuming process that is poorly suited to identifying true optimums, analyzing fundamental mechanics or diagnosing limiting factors. Existing models focus on control and have not shown an ability to predict the result of design changes. This manuscript presented a soft robot arm model that is generalizable across form factors and intended to be used for design. The model's generalizability means it can be used to evaluate design changes, prior to manufacturing an arm. The model was validated for planar and spatial arms, and it demonstrated an ability to predict the results of design changes, within the limits imposed by the model's assumptions. The model can predict internal stresses (caused by actuation) and external loads (e.g., gravity, friction, tip loads). The model was used to evaluate the loaded workspace of planar soft arms constructed with contracting actuator, which demonstrated that such arms are more powerful when pulling toward their initial midline.

This manuscript identified arm behaviors that are relevant to ancillary pursuits in developing and using soft robot arms. Soft arms under load were shown to have a nonconstant curvature and to compress under load, even if the loads were not inherently compressive. The most common soft arm kinematic model is piecewise constant curvature (PCC), which is only capable of capturing the deformed shape if each segment is modeled as multiple kinematic links with known curvatures and stretches. Further, any inverse kinematic model must be subject to compatibility constraints. An inverse kinematic model typically relates the desired tip position to a set of curvatures in each PCC segment, but without a compatibility constraint, there exists no guarantee that the soft arm can reach the required states. The development of a compatibility constraint that can be computed quickly is an open, and significant, challenge.

There are three limitations with the current model that are potential paths for future work. First, loads are currently limited to the bend plane. This limitation can be removed by extending the formulation from a beam to a more general rod theory. Rod theory requires a more extensive characterization of stiffnesses, but it may improve model capability. Second, the model is quasi-static, but it can be extended to a more complex dynamic formulation, in order to capture transient events, by characterizing the kinetic energy of the actuators and arm plates. The final model limitation is the exclusion of shear deformation

and bending stiffness. Bending stiffness can be included in the current formulation, but requires characterization of that stiffness across the strain-pressure domain. Shear can be included in beam models, such as in Timoshenko beam theory, assuming sufficient computational power and the relevant actuator shear stiffness characterizations. Future research may examine arm measurement techniques that accurately capture the shear strain, though measurement of highly deformable bodies remains challenging and requires equipment not standard to robotics laboratories. However, an alternative research direction is to consider whether shear is necessary, or desired, in soft arms. Shearing limited the stroke and force of the tested soft arms, and alternate designs with less shear may improve performance.

The ability to design capable robots to specific criteria is critical to soft robotics. While the inherent safety and compliance of soft robots shows clear potential, that potential has yet to be converted to functional, broadly capable soft robots. Acknowledged challenges remain in artificial muscle development, control and planning, but the potential of existing actuators to produce capable soft robot is unquantified, because no tools exist to quantify it. The model and analysis presented in this manuscript quantify some capabilities of soft arms constructed with McKibben actuators. The segment model is not limited to McKibben actuators, and can be used to evaluate arms constructed from other actuator types, once those actuators have been characterized. The model, coupled with a library of actuator characterizations, can be used to quantitatively and methodically address questions of soft arm capability.

# 7. Funding

This work was supported in part by the National Science Foundation, under award IIS-1734627 and CMMI-1653220.

## 8. Conflicts of Interest

The authors declare that there is no conflict of interest.

## 9. References

- [1] R. K. Katzschmann, J. DelPreto, R. MacCurdy, D. Rus, Exploration of underwater life with an acoustically controlled soft robotic fish, Science Robotics 3 (16) (2018).
- [2] K. C. Galloway, K. P. Becker, B. Phillips, J. Kirby, S. Licht, D. Tchernov, R. J. Wood, D. F. Gruber, Soft robotic grippers for biological sampling on deep reefs, Soft Robotics 3 (1) (2016).
- [3] W. McMahan, V. Chitrakaran, M. Csencsits, D. Dawson, I. D. Walker, B. A. Jones, M. Pritts, D. Dienno, M. Grissom, C. D. Rahn, Field trials and testing of the octarm continuum manipulator, in: Proceedings 2006 IEEE International Conference on Robotics and Automation, 2006. ICRA 2006., 2006, pp. 2336–2341. doi:10.1109/ROBOT.2006.1642051.
- [4] I. Godage, G. Medrano-Cerda, D. Branson, E. Guglielmino, D. Caldwell, Dynamics for variable length multisection continuum arms, The International Journal of Robotics Research 35 (6) (2016) 695–722.
- [5] C. Chou, B. Hannaford, Measurement and modeling of mckibben pneumatic artificial muscles, IEEE Transactions on Robotics and Automation 12 (1) (1996) 90–102.
- [6] G. Krishnan, J. Bishop-Moser, C. Kim, S. Kota, Kinematics of a generalized class of pneumatic artificial muscles, Journal of Mechanisms and Robotics 7 (4) (2015).
- [7] K. Oliver-Butler, J. Till, C. Rucker, Continuum robot deflection under external loads and prescribed tendon displacements, IEEE Transactions on Robotics Advance online publication. doi: 10.1109/TRO.2018.2885923.
- [8] M. Follador, M. Cianchetti, C. Laschi, Development of the functional unit of a completely soft octopuslike robotic arm, 4th IEEE RAS & EMBS International Conference on Biomedical Robotics and Biomechatronics (BioRob 2012) (2012).
- [9] B. Mosadegh, P. Polygerinos, C. Keplinger, S. Wennstedt, R. Shepherd, U. Gupta, J. Shim, K. Bertoldi, C. Walsh, G. Whitesides, Pneumatic networks for soft robotics that actuate rapidly, Advanced Functional Materials 24 (15) (2014) 2163–2170.
- [10] F. Connolly, C. Walsh, K. Bertoldi, Automatic design of fiber-reinforced soft actuators for trajectory matching, Proceedings of the National Academy of Sciences of the United States of America (PNAS) 114 (1) (2017) 51–56.
- [11] F. Daerden, D. Lefeber, Pneumatic artificial muscles: actuators for robotics and automation, European Journal of Mechanical and Environmental Engineering 47 (1) (2002) 11–21.
- [12] S. Kim, C. Laschi, B. Trimmer, Soft robotics: a bioinspired evolution in robotics, Trends in Biotechnology 35 (5) (2013) 287–294.
- [13] E. Guglielmino, N. Tsagarakis, D. Caldwell, An octopus anatomy-inspired robotic arm, IEEE/RSJ International Conference on Intelligent Robots and Systems (IROS 2010) (2010).
- [14] Y. Ansari, M. Manti, E. Falotico, M. Cianchetti, C. Laschi, Multiobjective optimization for stiffness

- and position control in a soft robot arm module, IEEE Robotics and Automation Letters 3 (2018).
- [15] A. Marchese, R. Tendrake, D. Rus, Dynamics and trajectory optimization for a soft spatial fluidic elastomer manipulator, The International Journal of Robotics Research 35 (8) (2016) 1000–1019.
- [16] M. Cianchetti, T. Ranzani, G. Gerboni, I. D. Falco, C. Laschi, A. Menciassi, Stiff-flop surgical manipulator: mechanical design and experimental characterization of the single module, IEEE/RSJ International Conference on Intelligent Robots and Systems (IROS 2013) (2013).
- [17] M. Giannaccini, C. Xiang, A. Atyabi, T. Theodoridis, S. Nefti-Meziani, S. Davis, Novel design of a soft lightweight pneumatic continuum robot arm with decoupled variable stiffness and positioning, Soft Robotics 5 (1) (2018).
- [18] W. Zhang, P. Polygerinos, Distributed planning of multi-segment soft robotic arms, in: 2018 Annual American Control Conference (ACC), IEEE, 2018, pp. 2096–2101.
- [19] B. Jones, I. Walker, Kinematics for multisection continuum robots, IEEE Transactions on Robotics 22 (1) (2006).
- [20] I. Godage, D. Branson, E. Guglielmino, G. Medrano-Cerda, D. Caldwell, Shape function-based kinematics and dynamics for variable length continuum robotic arms, IEEE International Conference on Robotics and Automation (2011) 452–457.
- [21] H. B. Gilbert, I. S. Godage, Validation of an extensible rod model for soft continuum manipulators, IEEE International Conference on Soft Robotics (RoboSoft) (2019).
- [22] F. Renda, F. Boyer, J. Dias, L. Seneviratne, Discrete cosserat approach for multisection soft manipulator dynamics, IEEE Transactions on Robotics 34 (2018) 1518 1533.
- [23] A. Sipos, P. Várkonyi, The longest soft robotic arm, International Journal of Non-Linear Mechanics (2019). doi:10.1016/j.ijnonlinmec.2019.103354.
- [24] Y. Shapiro, K. Gabor, A. Wolf, Modeling a hyperflexible planar bending actuator as an inextensible euler-bernoulli beam for use in flexible robots, Soft Robotics 2 (2) (2015).
- [25] K. Xu, N. Simaan, Analytic formulation for kinematics, statics, and shape restoration of multibackbone continuum robots via elliptic integrals, Journal of Mechanisms and Robotics 2 (1) (2010).
- [26] D. Trivedi, A. Lotfi, C. D. Rahn, Geometrically exact models for soft robotic manipulators, IEEE Transactions on Robotics 24 (4) (2008) 773–780.
- [27] G. Olson, S. Chow, A. Nicolai, C. Branyan, G. Hollinger, Y. Mengüç, A generalizable equilibrium model for bending soft arms with longitudinal actuators, The International Journal of Robotics Research 0 (0) (2019). doi:10.1177/0278364919880259.
- [28] G. Olson, B. Woronowicz, Y. Menguc, Characterization of a class of soft bending arms, IEEE International Conference on Soft Robotics (RoboSoft 2019) (2019) 462–469.
- [29] W. Zhang, P. Polygerinos, Distributed planning of multi-segment soft robotic arms, Annual American

Control Conference (ACC 2018) (2018).

- [30] S. Antman, Nonlinear Problems of Elasticity, Springer, 1995.
- [31] M. Doumit, A. Fahim, M. Munro, Analytical modeling and experimental validation of the braided pneumatic muscle, IEEE Transactions on Robotics 25 (6) (2009) 1282–1291.
- [32] B. Tondu, Modelling of the mckibben artificial muscle: A review, Journal of Intelligent Material Systems and Structures 23 (3) (2012) 225–253.
- [33] G. Olson, H. Manjarrez, J. A. Adams, Y. Menguc, Experimentally identified models of mckibben soft actuators as primary movers and passive structures, Preprint (2020). doi:10.13140/RG.2.2.31749.29920.

# Appendix A. Actuator Characterization

The actuator force characterization was produced experimentally, by measuring force for a large number of strain-pressure combinations in each region of the strain-pressure space (Figure 4). Tests were completed on a Mark-10 ESM 1500 motorized test stand with a 50 N load cell (model MR03-10). The test stand has a position resolution of 0.02 mm, and the load cell has an accuracy of 0.075 N and resolution of 0.02 N. Pressure was measured with a Honeywell TruStability 30 psi (200 kPa) pressure sensor read through an Arduino. The pressure sensor had a resolution of 0.2 kPa and an accuracy of  $\pm 0.55$  kPa.

Strain-pressure regions with a tensile reaction force (even in the strain was nominally compressive) were tested on single actuators with keys attached. Actuators were connected to the test stand at the bottom, near the pressure inlet, and were connected to the load cell at the top. Five samples were tested to capture the range of forces possible due to actuator variance.

Strain-pressure regions with a compressive reaction force were tested as part of an arm. The arm had four actuators equally distributed around a circle. The bottom plate of the arm was connected to the test stand, and a small platen was used to compress the top plate. Pressures that resulted in tensile loads pulled the arm away from the platen, which meant that forces only registered when compressive. Testing compressive regions in an arm prevented actuator column buckling during testing. Actuator column buckling in the arm is prevented during use by the reinforcing plates, and the plates were used for the same purpose

during testing. Smooth rods were placed around the plates to further guarantee that the arm did not buckle during testing. Eight samples were used in total during compression testing, grouped into three sets of four.

The fit forms used are purely experimental, and are not proven to follow physical trends in actuator behavior beyond the tested region. The forms were developed in prior work and are guaranteed to be self-consistent at region boundaries [33]. The coefficients specific to the actuators used in validation were developed as part of this work. The coefficients are given in Table A.5 along with an a root mean squared error for the fit.

Passive compression and extension were tested in a direct analog to tensile and compressive material testing. The passive compression results were fit to

$$F_C = k_{C,1}\varepsilon^4 + k_{C,2}\varepsilon^3 + k_{C,3}\varepsilon^2 + k_{C,4}\varepsilon, \tag{A.1}$$

and the passive extension results were fit to

$$F_E = k_{E,1}\varepsilon^3 + k_{E,2}\varepsilon^2 + k_{E,3}\varepsilon. \tag{A.2}$$

The fits are compared to the experimental data in Figure A.13(a) and (b). The primary driver of fit error is actuator variance.

The actuation region is defined as the region with contraction strains but a tensile reaction force. The region was tested by pressurizing actuators at set strains. Each actuator was tested in increments of 2 mm (approximately 1% strain) from nominal length until the actuator stopped producing a tensile force for pressures under 100 kPa. This test regime generally resulted in data for 30 strains. The force in the region was fit to

$$F_{AR}(\varepsilon, P) = k_{AR,1}(k_{AR,2} + \varepsilon)^2 (P - P_{FC}(\varepsilon)), \tag{A.3}$$

where the free contraction pressure  $P_{FC}$  was fit to

$$P_{FC} = k_{FC,1}\varepsilon^4 + k_{FC,2}\varepsilon^3 + k_{FC,3}\varepsilon^2 + k_{FC,4}\varepsilon. \tag{A.4}$$

The fits are compared to experimental data in Figure A.13(c) and (d). Only a subset of tested strains are shown in Figure A.13 to avoid overcrowding the plot.

Pressurized extension occurs when the tensile force applied to the actuator is greater than the force that can be produced by the actuator at that pressure and zero strain. The reaction force is a sum of passive extension and actuation. The region was tested using the same method as the actuation region, but with strains increments of 0.5%. The region was fit to

$$F_{PE} = F_E(\varepsilon) + k_{PE,1}(k_{PE,B} + k_{PE,2}\varepsilon)^2 P^{(1+k_{PE,3}\varepsilon)}.$$
 (A.5)

where  $F_E$  is given by Equation (A.2) and  $k_{PE,B}$  is a boundary constraint derived by equating force between the actuation region and pressurized extension at zero strain. The constraint is

$$k_{PE,B} = \frac{\sqrt{k_{AR,1}k_{AR,2}^2}}{k_{PE,1}}. (A.6)$$

The fits are compared to experimental data in Figure A.13(f).

Pressurized compression occurs when the compressive load is higher than the actuation region can support at a given pressure. The region is the most complex region to fit, because it displays multiple distinct behaviors. The region begins under the free contraction line in the strain-pressure space and extends left to the highest contraction strain tested. The regions are divided by the limit strain, which is defined as the strain that  $P_{max} = 100$  kPa produces zero force. The limit strain for the actuators used in this article is  $\varepsilon_{limit} = -0.274$ . Strains greater than  $\varepsilon_{limit}$ , combined with pressures less than the free contraction pressure for the given strain, were fit with

$$F_{PC-A} = F_C(\varepsilon), \quad \{P : 0 \le P \le P_{crit}\},\tag{A.7}$$

$$F_{PC-A} = F_C(\varepsilon) + k_{PC-A,1} (k_{PC-A,2} + \varepsilon)^2 (P - P_{crit}), \quad \{P : P \ge P_{crit}\}. \quad (A.8)$$

 $F_C$  is given by Equation (A.1), and  $P_{crit}$  is a boundary compatibility constraint calculated with

$$P_{crit} = \frac{F_C}{k_{PC-A,1}(k_{PC-A,2} + \varepsilon)^2} + P_{FC}(\varepsilon). \tag{A.9}$$

Table A.5: Actuator characterization fit coefficients and error.

Region $(\#)$	$k_{\#,1}$	$k_{\#,2}$	$k_{\#,3}$	$k_{\#,4}$	Error
С	265	321	126	21.9	0.14 N
E	9.00e4	836	62.6	_	0.82 N
AR	1.04	0.51	_	_	0.63 N
FC	3.46e4	5.99e3	-1.03e3	-396	2.76 kPa
PE	1.96	-3.17	4.23	_	0.82 N
PC-A	0.637	0.453	-	_	0.18 N
PC-B	3.70	_	_	_	0.23 N

The second region, PC-B, includes all strains less than  $\varepsilon_{limit}$ . The reaction force is compressive at every pressure less than  $P_{max}$ . The reaction force in this region below  $P_{crit}$  is

$$F_{PC-B} = F_C(\varepsilon), \quad \{P : 0 \le P \le P_{crit}\},\tag{A.10}$$

in order to maintain continuity with  $F_{PC-A}$  at the boundary. The force for pressures above  $P_{crit}$  was fit with

$$F_{PC-B} = F_C(\varepsilon) + k_{PC-B,B}(-\varepsilon_{crit} + \varepsilon)^2 (P - P_{crit})$$
(A.11)

for  $\{\varepsilon : \varepsilon_{limit} \ge \varepsilon \le \varepsilon_{crit}\}$ . The actuator behavior changes at the critical strain  $\varepsilon_{crit}$  as the sheath passes the neutral angle. The critical strain for the actuators used in this article was  $\varepsilon_{crit} = -0.303$ . The actuator acts as an extending actuator at strains less than  $\varepsilon_{crit}$ , and the force was modeled by

$$F_{PC-B} = F_C(\varepsilon) - k_{PC-B,1}(-\varepsilon_{crit} + \varepsilon)^2 (P - P_{crit}). \tag{A.12}$$

The boundary constraint between Region PC-A and PC-B is

$$k_{PC-B,B} = \frac{k_{PC-A,1}(k_{PC-A,2} + \varepsilon_{limit})^2}{(-\varepsilon_{crit} + \varepsilon_{limit})^2}.$$
(A.13)

The fit is compared to the experimental results in Figure A.13(e).

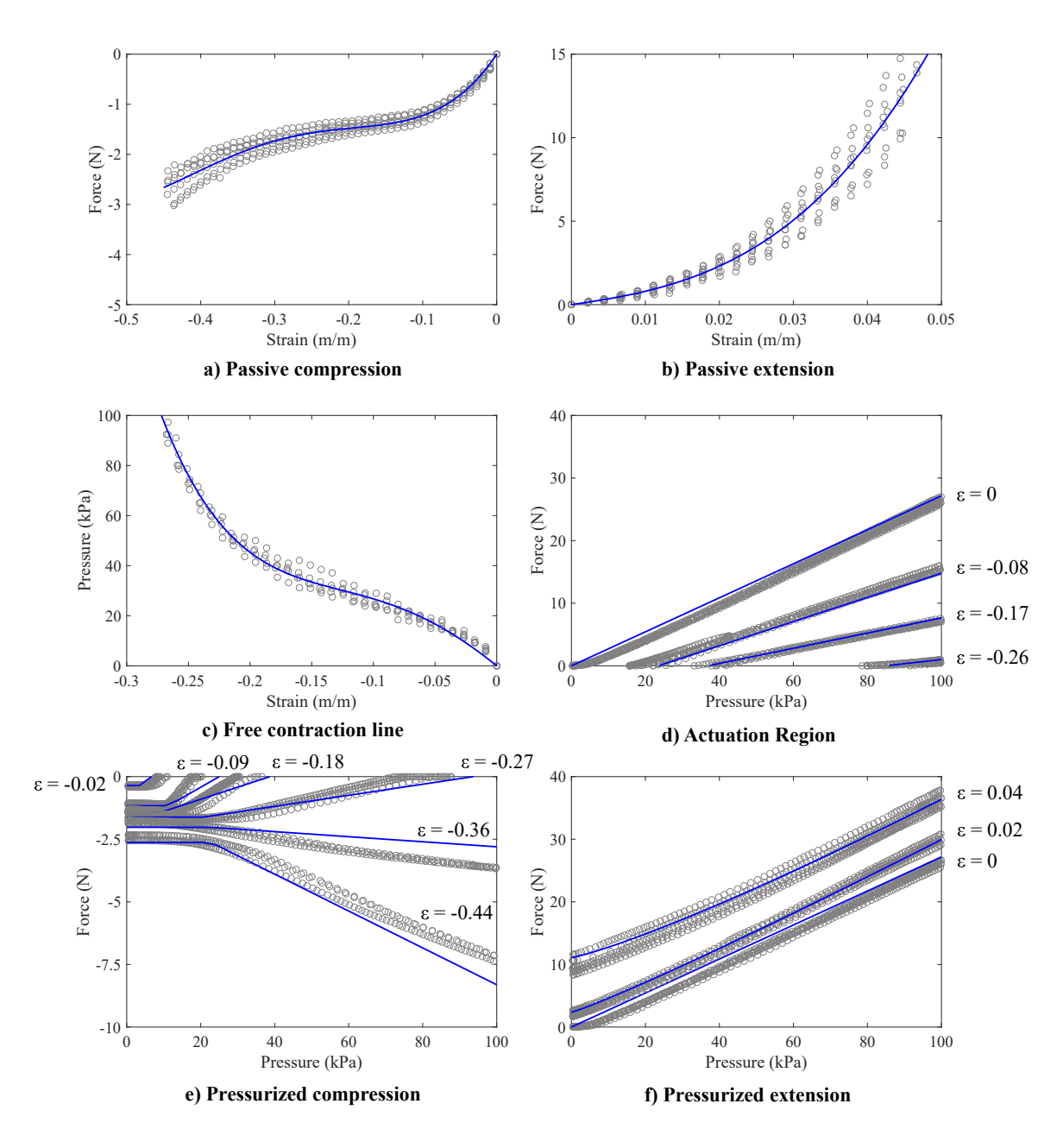


Figure A.13: Comparison of experimental measurements of actuator force and actuator fit predictions, for each region and line in the strain-pressure space.

# Appendix B. Neutral Axis Formulation

This appendix describes a formulation of the model's kinematics in terms of the neutral axis. The validation results presented in Section 4 used this formulation, which gives a result equivalent to the base curve formulation in Section 3. The neutral axis formulation describes segment shape using a neutral axis curvature and height from the base curve, while the base curve formulation use a base curvature and stretch. The neutral axis formulation does not require a stretch, because the stretch is unity at this axis by definition. There is a singularity in the neutral axis formulation when curvature changes direction, because the neutral axis height passes from  $-\infty$  to  $\infty$ , or vice versa. This singularity can impede convergence of a numerical solver, but can be accommodated by disallowing large neutral axis heights (> 1m in this manuscript) in the solution guess.

The arm segment exists within a general coordinate system, which is chosen to be aligned with Actuator 1 (Figure 3). A second coordinate system is established, rotated from the first about the z-axis by the bend angle,  $\theta_b$ . This new coordinate system, x' - z', aligns the x-axis with the bend plane (Figure 3(a), (d)). A third, moving, coordinate system given by  $\hat{e}_n$ ,  $\hat{e}_t$  is attached to the arm's base curve.  $\hat{e}_n$  is the unit normal vector to the base curve,  $\hat{e}_t$  is the unit tangent vector.

The base curve and neutral axis lie within the x'-z' plane (Figure 3(b)), and all curvature occurs within this plane. The undeformed neutral axis is parameterized by s, which extends to the actuator length L, and initially lies co-axial to the base curve. The arm's deformation is described by the curvature of the neutral axis (the inverse of bend radius r),  $\kappa_{NA}(s)$ , and its height from the base curve, h(s). By definition, the neutral axis does not experience strain. The deformed neutral axis is not assumed, or required, to lie at the arm's center, or even within its cross section.

The x'-z' coordinates of the base curve are required in order to calculate the internal reaction forces and moments from the applied load Q. The base curve's curvature and stretch,  $\lambda_c$ , can be determined from neutral axis's curvature and height. The stretch along

s is given by

$$\lambda_c(s) = 1 + h(s)\kappa_{NA}(s). \tag{B.1}$$

The base curvature,  $\kappa_c$ , is offset from the neutral axis curvature by the neutral axis height:

$$\frac{1}{\kappa_c} = \frac{1}{\kappa_{NA}} + h(s). \tag{B.2}$$

Determining the base curve's x'-z' coordinates from curvatures is simpler than for a general curve, because the base curve is twist free and confined to one plane. Equation (2) simplifies to

$$\begin{bmatrix} z' \\ x' \end{bmatrix} (s) = \int_0^s \begin{bmatrix} \lambda_c(S) \cos \theta(S) \\ \lambda_c(S) \sin \theta(S) \end{bmatrix} dS.$$
 (B.3)

The strains experienced by each actuator, at each point along s, are also determined kinematically. The strain is zero at the neutral axis and increases linearly with height above or below the axis. The  $i^{th}$  actuator's absolute position vector is

$$\vec{a}_i = (x_i, y_i), \tag{B.4}$$

but the relative height above the neutral axis,  $H_i(s)$ , varies with bend direction and along the arm length. Actuator height in the bend plane can be determined with the scalar projection of the actuator's position vector onto unit vectors that align with axes of the rotated frame x' - y'. The unit vector that aligns with the x'-axis is

$$\hat{e}_n = (\cos \theta_b, \sin \theta_b), \tag{B.5}$$

and the unit vector that aligns with the y'-axis is

$$\hat{e}_b = (-\sin\theta_b, \cos\theta_b). \tag{B.6}$$

These unit vectors are calculated once per segment, because each segment bends in one plane. The  $i^{th}$  actuator's height above the neutral axis is the difference between the neutral axis location and the actuator's absolute height projected into the bend plane (Figure 3(d)):

$$H_i(s) = h(s) - \vec{a}_i \cdot \hat{e}_n. \tag{B.7}$$

 $W_i$ , the distance between the arm's center and the  $i^{th}$  actuator in the plane perpendicular to the bend, is

$$W_i = \vec{a}_i \cdot \hat{e}_b. \tag{B.8}$$

Uniaxial strain induced by shear-free bending changes linearly through the cross section, at a rate determined by the curvature. The strains at each actuator are

$$\varepsilon_i(s) = H_i(s)\kappa_{NA}(s).$$
 (B.9)